crucially, when the sample position was moved a different phase was observed in a nonirradiated section of the sample. These two facts suggest that the sample was prone to beam damage and possibly that beam heating was also occurring. Thus the transition temperatures observed are not reliable, but data collected from a section of a sample that was only in the X-ray beam for a short time should provide reliable phase information. Beam damage is thought to be predominate in systems exhibiting hydrogen bonding, and acts to destroy those bonds.[74] Thus the appearance of the high temperature phase at lower temperatures than expected may suggest that hydrogen bonding is an important factor in formation of the low temperature phase.

4.3.2 Neutron Powder Diffraction

The neutron diffraction data show the same HT and LT phases as the X-ray data and once again the HT phase was observed at all temperatures. The maintained presence of the high temperature phase at low temperatures may be a result of disorder being frozen into the system due to the cooling rate, although it is possible that even with an infinitely slow cooling rate some disorder may remain in the system. Observation of the diffraction data shows that reflections from the low temperature phase appear at 90 K and reach full intensity at 80 K upon cooling. Upon heating they start to disappear at 85 K and are completely absent at 90 K. The observed transition temperatures are more reliable than those seen in the X-ray data, as neutron irradiation does not induce the same type of beam damage or heating as X-ray.

A theoretical study produced by Tekin et. al. suggested an ordered phase would exist in one of the space groups; $R\bar{3}$, $I4/m$, $C2/m$ or $Cmmm$, with the $R\bar{3}$ structure calculated to have the lowest energy.[44] None of the proposed sets of unit cell parameters allowed a good fit to the data, however doubling the parameters of the $R\bar{3}$ cell did allow a good fit to the data. Without any further knowledge of the

proposed structure, the space group $R\bar{3}$ is not a clear choice, there was no significant improvement in the fit of the Pawley refinement using either $R\bar{3}$ or its supergroup $R\bar{3}m$. In absence of any reason to lower the symmetry and given that it is also a subgroup of $Fm\bar{3}m$, the higher symmetry $R\bar{3}m$ was chosen. The final fit of the $R\bar{3}m$ cell to the neutron diffraction data is shown in Figure 4.4, the refined lattice parameters for the hexagonal cell are a = 15.92(3) Å and b = 32.3(2) Å with a volume V = 7304(52) Å^3. The uncertainties in these lattice parameters are huge and this reflects the broad peak shape which itself indicates significant strain in the sample. These uncertainties combined with the huge unit cell meant that attempts to solve the structure using the simulated annealing technique did not yield any useful results. Using computational methods to try and maximise the number of NH···Cl$^-$ interactions would probably be the best method to try and solve this structure.

The changes in lattice parameter of the HT phase with respect to temperature are shown in Figure 4.5, which highlights the lack of hysteresis in the neutron data. The change in lattice parameters suggest that the phase transition occurs between 70 K and 90 K, which agrees with the *prima facie* analysis. An interesting feature of the data is the expanded lattice of the HT phase when coexistent with the LT phase. It is proposed that formation of NH···Cl$^-$ bonds, in a manner analogous to the expansion of ice cf. water, cause this expansion of the lattice. This is strong evidence for dynamic disorder existing above the transition temperature in the high temperature phase. Unfortunately the diffraction data are not of sufficient quality to analyse this in more detail. Investigation of the low temperature phase shows a more normal volume expansion with increasing temperature, though without any structural information and given the large number of potential reflections contributing to the broad peaks, detailed analysis of these lattice changes is a moot point.

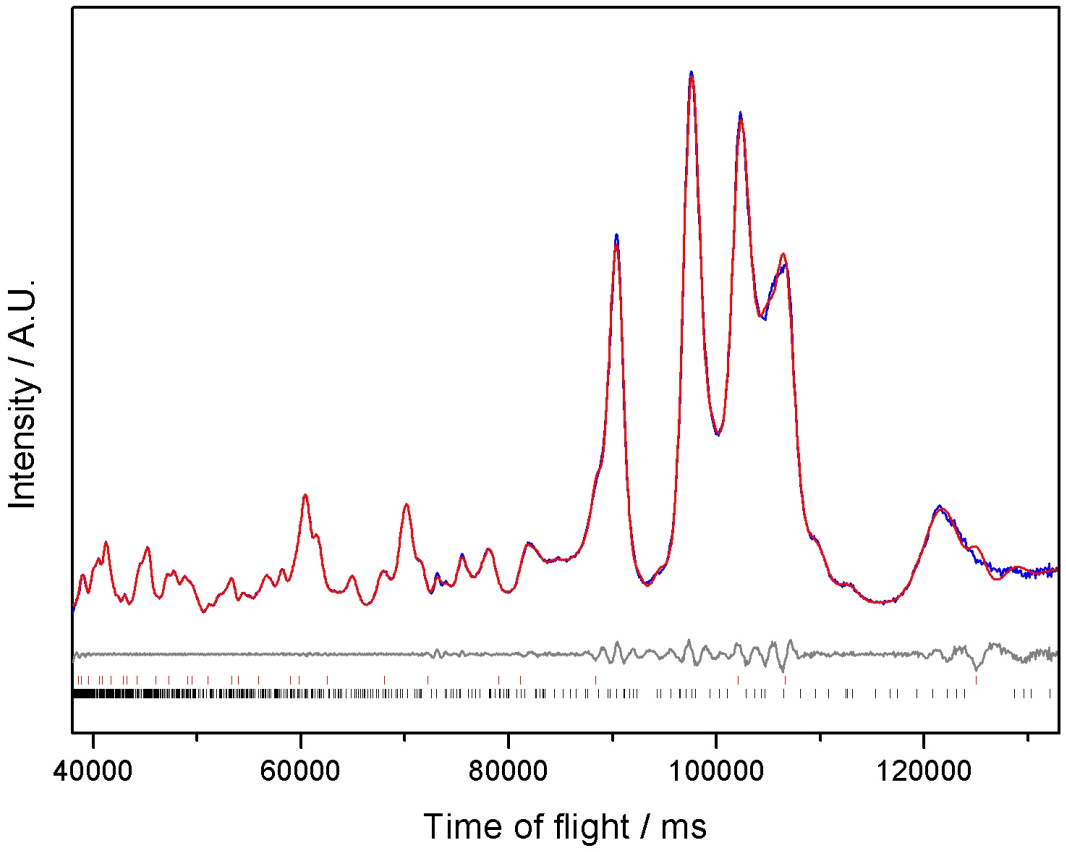

Figure 4.4: Final fit to the data for Pawley refinement of the $Mg(NH_3)_6Cl_2$ low temperature unit cell to neutron powder diffraction data, collected using HRPD bank 2 (90 °) at a temperature of 20 K. Experimental data are shown in blue, calculated in red with the difference in grey, tick marks show the expected positions of Bragg reflections with the high temperature phase in red and the low temperature phase in black.

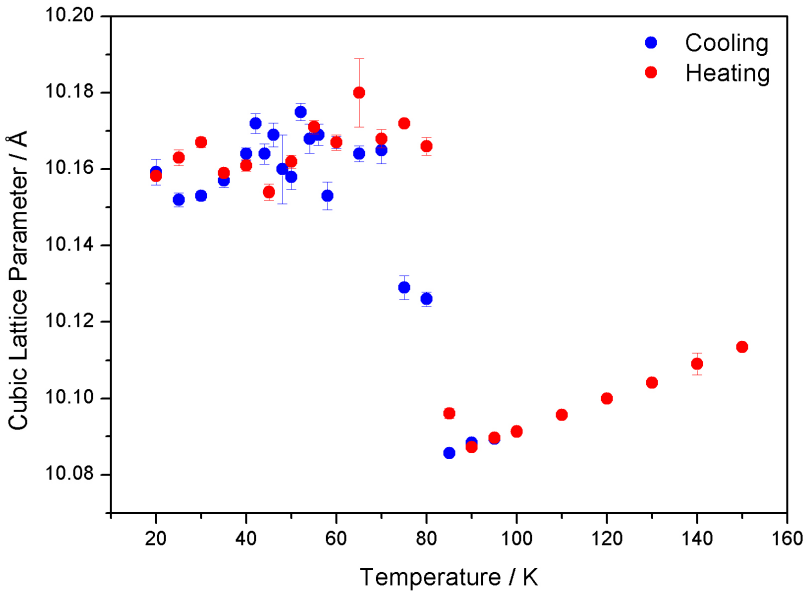

Figure 4.5: The lattice parameters of the $Mg(NH_3)_6Cl_2$ high-temperature phase between 20 K and 150 K, refined from neutron diffraction data collected using HRPD bank 2 (90 °).

4.4 Nuclear Magnetic Resonance

^{25}Mg NMR measurements were carried out at Durham University via the EPSRC solid-state NMR service and initial analysis was aided by Dr David Apperley. The purpose of these experiments was to investigate the influence of the anion on the Mg nuclei and Mg−N bonding in MgX_2 and $Mg(NH_3)_6X_2$. The very low resonant frequency of the ^{25}Mg nucleus means that it can be hard to observe using NMR as most spectrometers are unable to operate at such a low frequency. Thus, and given the nature of shared resources and the requirements of this Thesis, it was not possible to follow some of the more interesting spectroscopic results with further investigation.

The spectra of MgI_2 and all $Mg(NH_3)_6X_2$ each show a narrow symmetric line, typified by the $Mg(NH_3)_6Cl_2$ spectra shown in Figure 4.6 (the remaining spectra are shown in Appendix E.1 to E.3). The narrow and symmetric lines shows that there

is no second-order quadrupolar broadening so the magnesium must be in a high-symmetry (octahedral) environment. This is consistent with the K_2PtCl_6 structures of $Mg(NH_3)_6X_2$ and the CdI_2 structure of MgI_2.

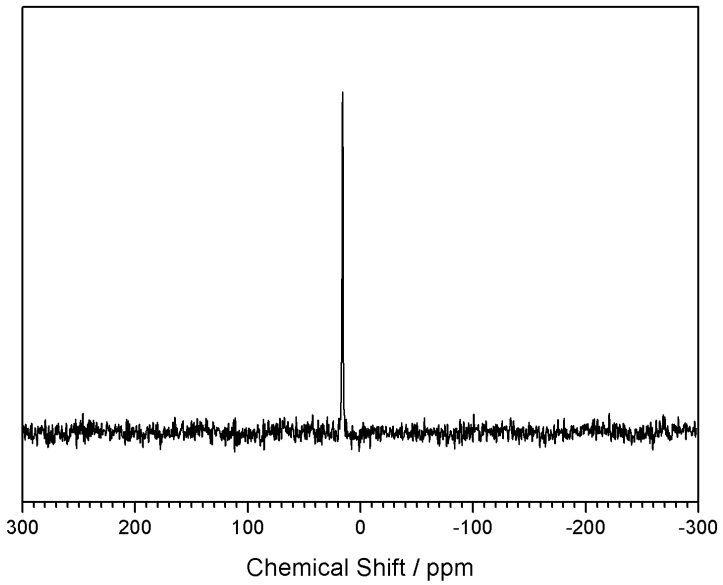

Figure 4.6: The ^{25}Mg NMR spectra of $Mg(NH_3)_6Cl_2$, showing a sharp line at 15.921 ppm (referenced to a 1 M solution of $Mg(H_2O)_6Cl_{2\,(aq)}$).

The spectra of $MgBr_2$ is shown in Figure 4.7. As with MgI_2 there is a single line but in this case second order quadrupolar broadening is observed. This suggests a lower symmetry environment than that found in MgI_2 but one that is still axially symmetric. This is not consistent with the crystal structure, as $MgBr_2$ also adopts the CdI_2 structure under these conditions and changing the proximity of neighbouring ions alone should not introduce any second order effects. This is certainly an interesting spectra, though for the purposes of this work the region of the chemical shift is the most important result.

The spectra of $MgCl_2$ is shown in Figure 4.8, again a single sharp line is observed, but with the presence of 2 additional peaks. It does not appear that these peaks are part of the quadrupolar bandshape, and it is likely that they belong either to

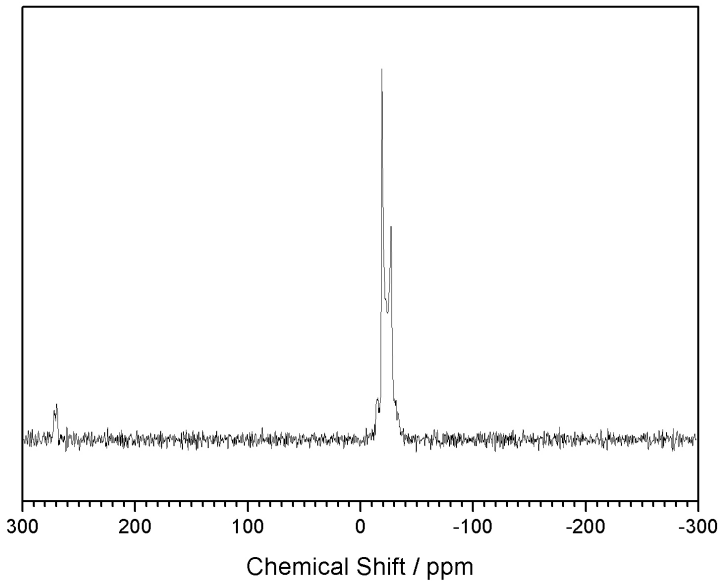

Figure 4.7: The ^{25}Mg NMR spectra of $MgBr_2$, showing sharp lines at 19.000 ppm and -27.111 ppm (referenced to a 1 M solution of $Mg(H_2O)_6Cl_{2\,(aq)}$).

a secondary phase or an impurity. There is a broad signal underlying the narrow lines that suggests some disorder in the system and may also be associated with an impurity. If this sample, or the $MgBr_2$ sample, did contain impurities then they should also appear in the spectra of the ammines, that they don't suggests the presence of disorder that still allows conversion to the ammine, that impurities were introduced to the sample during pre-measurement handling, or that the impurities were removed during formation of the ammine. Once again the significant result for this work is the region of the chemical shift.

It was not possible to obtain a spectrum from MgF_2. This is likely due to a much higher quadrupole coupling constant than for the rest of the group resulting in a signal that is more diffuse or broad and difficult to detect. Dipolar coupling to fluorine may add additional line broadening that complicates matters further.

A summary of all NMR data is given in Table 4.3. In the MgX_2 series, the ^{25}Mg chemical shift was observed to decrease with increasing atomic number of the

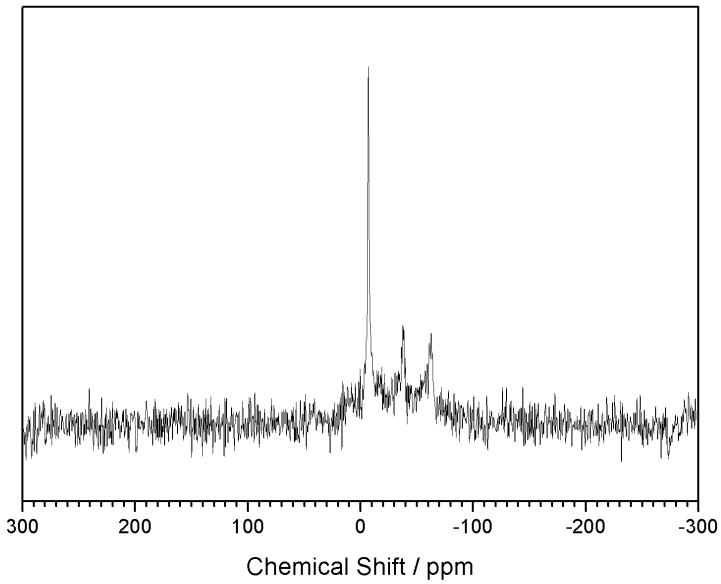

Figure 4.8: The ^{25}Mg NMR spectra of $MgCl_2$, showing a sharp line at -6.909 ppm (referenced to a 1 M solution of $Mg(H_2O)_6Cl_{2\,(aq)}$).

anion X. This decrease in chemical shift is indicative of an increase in diamagnetic shielding of the Mg cation, and hence an increase in the electron density around the Mg nucleus. This is a result of the change in electronegativity of the anion, with the larger less electronegative anions allowing a greater electron density to reside on the Mg nuclei.

The chemical shifts seen in the $Mg(NH_3)_6X_2$ series are shifted downfield relative to those in MgX_2, this corresponds to a lower electron density on the Mg nucleus in $Mg(NH_3)_6X_2$ than in the corresponding MgX_2. This reduced electron density most probably arises as the bulk of the electron density between the bonded Mg and N resides nearer to the more electronegative N atom.

Within the $Mg(NH_3)_6X_2$ series, the chemical shift decreases with increasing atomic number of X. This trend is the same as that observed in MgX_2 though an order of magnitude smaller. The small increase in Mg−N bond lengths discussed in Section 4.2.1 corroborate this effect, as increasing the electron density of the Mg^{2+}

cation will result in a weaker and longer bond. However, the differences in chemical shifts and Mg−N bond lengths of the $Mg(NH_3)_6X_2$ series are very small (covering a range of 0.8 ppm and 0.02 Å respectively), thus varying the anion does not appear to have any significant effect on the strength of the Mg−N bond.

Table 4.3: Summary of ^{25}Mg data for the MgX_2 and $Mg(NH_3)_6X_2$ series, chemical shifts referenced to a 1 M solution of $MgCl_2(H_2O)_{6\,(aq)}$.

Compound	Chemical Shift ppm	Compound	Chemical Shift ppm
$MgCl_2$	-6.9	$MgCl_2(NH_3)_6$	15.9
$MgBr_2$	-19.0	$MgBr_2(NH_3)_6$	15.2
MgI_2	-81.1	$MgI_2(NH_3)_6$	15.1

4.5 Thermogravimetric Analysis

Thermogravimetric analysis of $Mg(NH_3)_6X_2$ (X = Cl, Br, I) was carried out using the procedure described in Section 2.11.1. Measurements were carried out using a heating rate of 2 °Cmin^{-1} under a 1 bar argon atmosphere with a flow rate of 5 mlmin^{-1}. A comparison of each set of data is shown in Figure 4.9 and summarised in Table 4.4. Figure 4.10 shows each mass loss with the first derivative of the mass loss with respect to time ($\frac{dm}{dt}$) also plotted, these data are also summarised in Table 4.4. The derivative plots show that ammonia loss occurs in a three step process for each compound. These three steps have mass losses consistent with the process described in (Section 1.4) Equation 1.7, that is the evolution of 4 (T = T_1) and sequentially 2 × 1 (T = T_2 and T = T_3) ammonia molecules. The temperature required for each decomposition step is seen to increase down the halide group. It appears that the lifetime of the $Mg(NH_3)X_2$ intermediates decreases with increasing atomic number of X. A clear stability plateau may be observed in the desorption step for $Mg(NH_3)_2Cl_2$ to $Mg(NH_3)Cl_2$, which is less well defined for $Mg(NH_3)_2Br_2$

to $Mg(NH_3)Br_2$ and difficult to distinguish for $Mg(NH_3)_2I_2$ to $Mg(NH_3)I_2$. These trends are discussed further in Section 4.8.1.

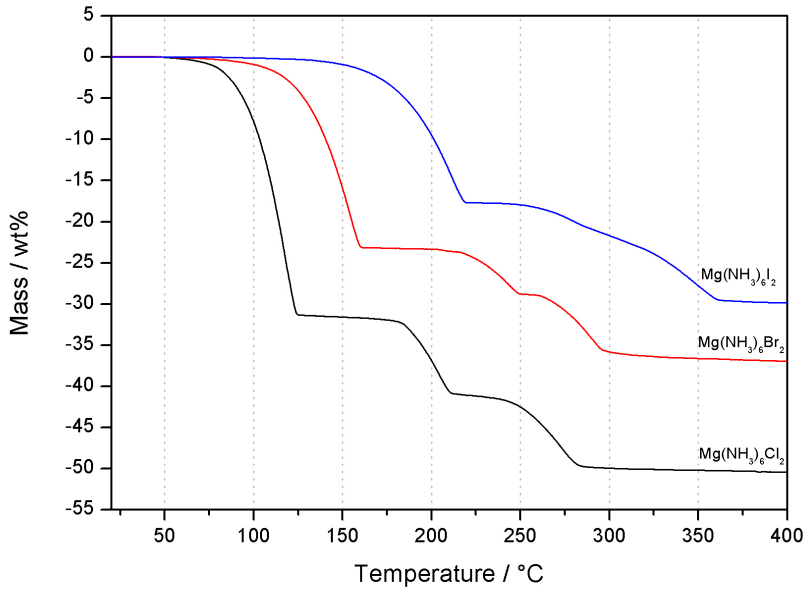

Figure 4.9: Mass loss of $Mg(NH_3)_6Cl_2$ as a function of temperature for in black, $Mg(NH_3)_6Br_2$ in red and $Mg(NH_3)_6I_2$ in blue.

Table 4.4: A summary of TGA data on the decomposition of $Mg(NH_3)_6X_2$.

Starting Compound	Desorption Step 1			Desorption Step 2			Desorption Step 3		
	T_{1o}	T_{1p}	wt%	T_{1o}	T_{1p}	wt%	T_{1o}	T_{1p}	wt%
$Mg(NH_3)_6Cl_2$	98	117	32	187	204	10	250	274	9
$Mg(NH_3)_6Br_2$	130	155	23	223	243	6	270	292	9
$Mg(NH_3)_6I_2$	182	212	18	na	282	na	na	349	na

Figure 4.11 shows a linear relationship between the anionic radii and the peak rate of desorption (T_p) for each of the three desorption steps, T_1, T_2 and T_3. The gradients of the lines of best fit are approximately equal for T_2 and T_3 (197 KÅ^{-1}), whilst that for T_1 is greater (275 KÅ^{-1}). The most appropriate analysis of these data considers all data presented in this Chapter, and is discussed in Section 4.8.1.

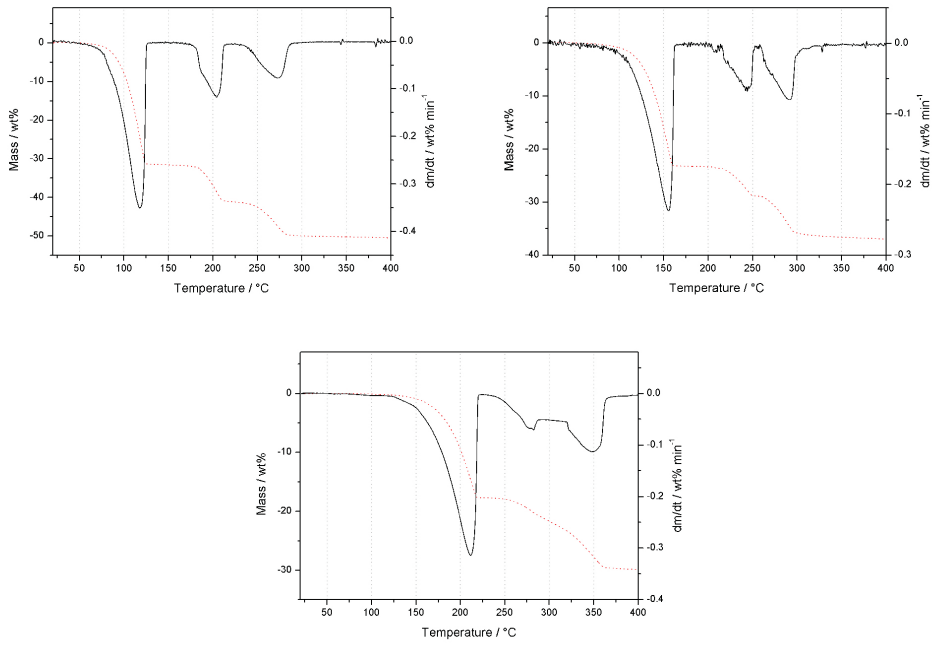

Figure 4.10: Mass loss as a function of temperature in red and the change in mass loss with respect to time (in this case $T = f(t)$) ($\frac{dm}{dt}$) in black for (from lop left to bottom) $Mg(NH_3)_6Cl_2$, $Mg(NH_3)_6Br_2$ and $Mg(NH_3)_6I_2$.

4.6 Inelastic Neutron Scattering

Inelastic neutron spectroscopy data were collected using TOSCA at ISIS. Samples of $Mg(NH_3)_6Cl_2$, $Mg(NH_3)_6Br_2$, and $Mg(NH_3)_6I_2$ were produced as described in Section 2.5 and loaded into aluminium sample holders in an argon atmosphere glove box. The spectra of all three compounds are shown in Figure 4.12, a large amount of common features reflect their structural similarity though to gain a better understanding of them it was necessary to model the data using DFT and aClimax. INS data were collected at 20 K, (as seen in Section 4.3) two phases of $Mg(NH_3)_6Cl_2$ coexist at this temperature and this is assumed to be the case for $Mg(NH_3)_6Br_2$ and $Mg(NH_3)_6I_2$. As the structure of the low temperature phase remains elusive and it is not possible to model the disordered phase[ii], any analysis becomes increasingly complicated. However, the fact that the disordered phase remains at low temper-

[ii]Within the computational limits of using a sensible amount processor time.

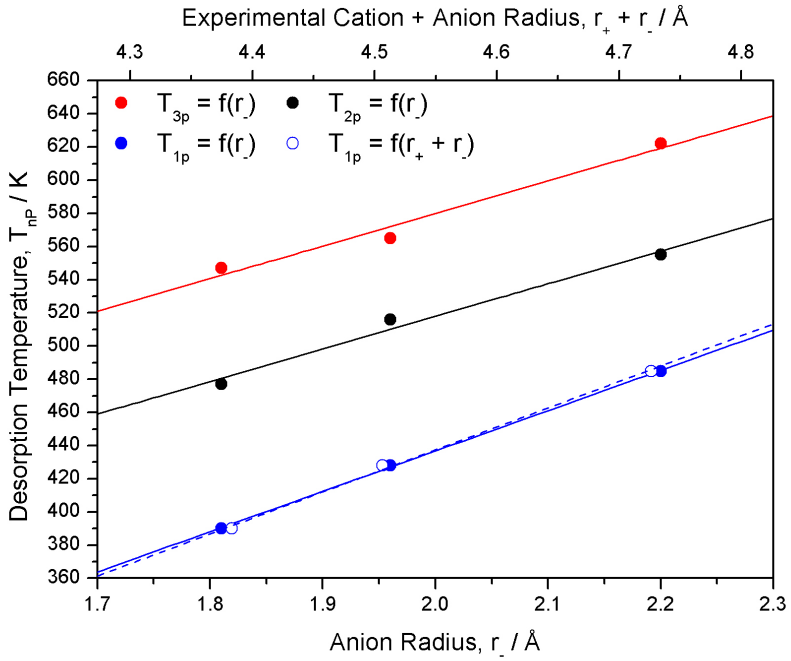

Figure 4.11: A plot of T_{nP} against ionic radii the X^- in $Mg(NH_3)_6X_2$ (X = Cl, Br, I). The lower x-axis shows the reported radii of X^-,[105] whilst the upper axis shows the radii of the cation plus anion as calculated from the X-ray powder diffraction data. The lines show linear fits to the data.

atures means a range of NH_3 orientations will exist in the solid. Simply modelling the data using the high-temperature cubic structure of $Mg(NH_3)_6Cl_2$ with an arbitrary set of ammonia orientations produces a calculated spectra, shown in Figure 4.13, that agrees strongly with the observed spectra. Analysing these simply calculated phonon modes should allow for reasonable assignment of modes seen in the experimental spectra, without the need for the more rigorous calculation required to find the most stable low temperature structure. A full description of the calculated modes is given in Appendix D.2.

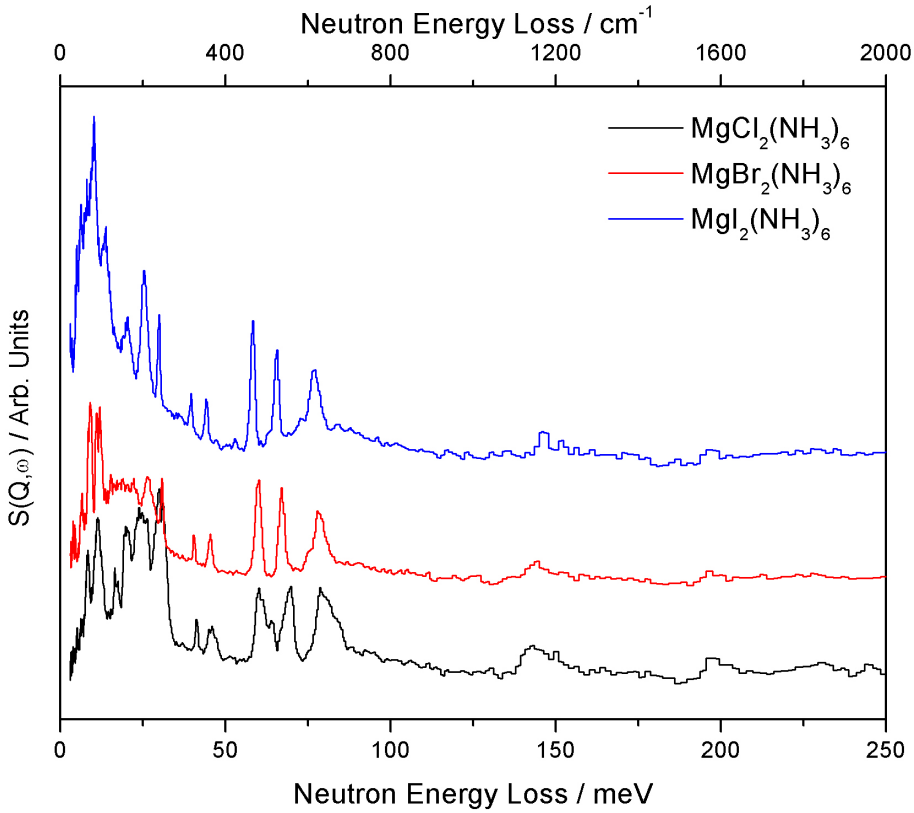

Figure 4.12: The INS spectra of $Mg(NH_3)_6Cl_2$ (black), $Mg(NH_3)_6Br_2$ (blue) and $Mg(NH_3)_6I_2$ (red), data were collected using TOSCA at a temperature of 20 K.

Figure 4.14 highlights a number of common modes that are observed to move as the anion is changed. All the labelled modes are detailed in Table 4.5 and relate to motion of NH_3 molecules in a manner associated with libration for modes 1 and 2; rocking (with some minor libration) for 3, 4, and 5, and; an umbrella

motion for 6. The range of the observed shifts varies from 14 cm^{-1} to 95 cm^{-1}, and while at the lower end the magnitude of the shifts may be outside the resolution of the instrument ($\delta\omega/\omega \approx 1.5$ %), the trends are still compelling. The decrease in energy of rotational modes with increasing anion size suggests that there is a small but significant NH···X^- interaction. The lower charge densities of the larger anions reduce the electrostatic strength of this interaction and thus the rotational energy barrier is reduced. The movement of the rocking and bending modes can be explained by considering a molecular orbital description of the bonding. Figure 4.15 shows how the NHX angle of a hydrogen bond is important in allowing maximum overlap between the N−H σ^* and the appropriate X^- p orbitals. The closer to 180 ° the bond is then the greater the potential orbital overlap and the stronger it becomes. The rocking modes (3 – 5) cause a reduced overlap of the orbitals, hence they decrease in energy as the anion size increases for the same reason that the rotational modes do: the weaker bonds of the larger anions are easier to disrupt. Mode 5 shifts 95 cm^{-1} compared to 24 cm^{-1} and 35 cm^{-1} for modes 3 and 4, because it involves significant movement of all 6 ammonia molecules rather than modes 3 and 4 that involve significant movement of only 2 ammonia molecules, thus the magnitude of the shift seen for mode 5 is a factor of 3 greater. The umbrella mode (6) follows a reversed trend, it increases in energy as the size of the anion increases, the reason for this is that the umbrella motions bring the N−H σ^* orbitals towards the same plane as the appropriate X^- p orbitals. Though the orbitals may not be physically able to move into the same plane, the angle of incidence between the σ^* orbital and the relevant p orbital is reduced. This will have a stabilising effect, so in the case of the smaller anions where there is a stronger bonding interaction, this mode is lowered in energy.

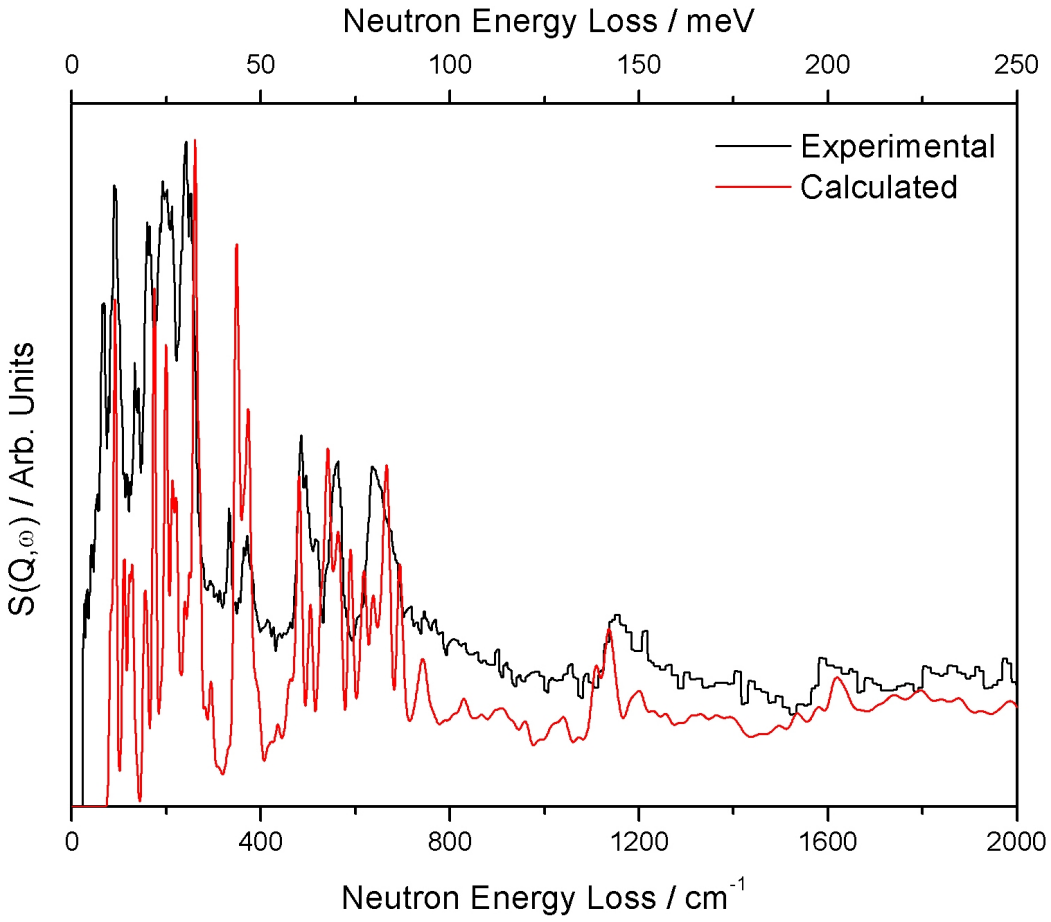

Figure 4.13: The experimentally observed (black) and calculated (red) INS spectra of $Mg(NH_3)_6Cl_2$.

Table 4.5: The observed positions and descriptions of selected modes in INS spectra for $Mg(NH_3)_6X_2$.

Mode Description	$Mg(NH_3)_6Cl_2$ ω / cm^{-1}	$Mg(NH_3)_6Br_2$ ω / cm^{-1}	$Mg(NH_3)_6Br_2$ ω / cm^{-1}
1) Single NH_3 rotation	333	327	319
2) Multiple NH_3 rotations and Mg−N breathing	370	365	354
3) In-phase, off N−H axis rocking	495	482	470
4) Anti-phase, off N−H axis rocking	563	541	528
5) All NH_3 molecules rocking	641	628	546
6) NH_3 umbrella modes	1155	1161	1178

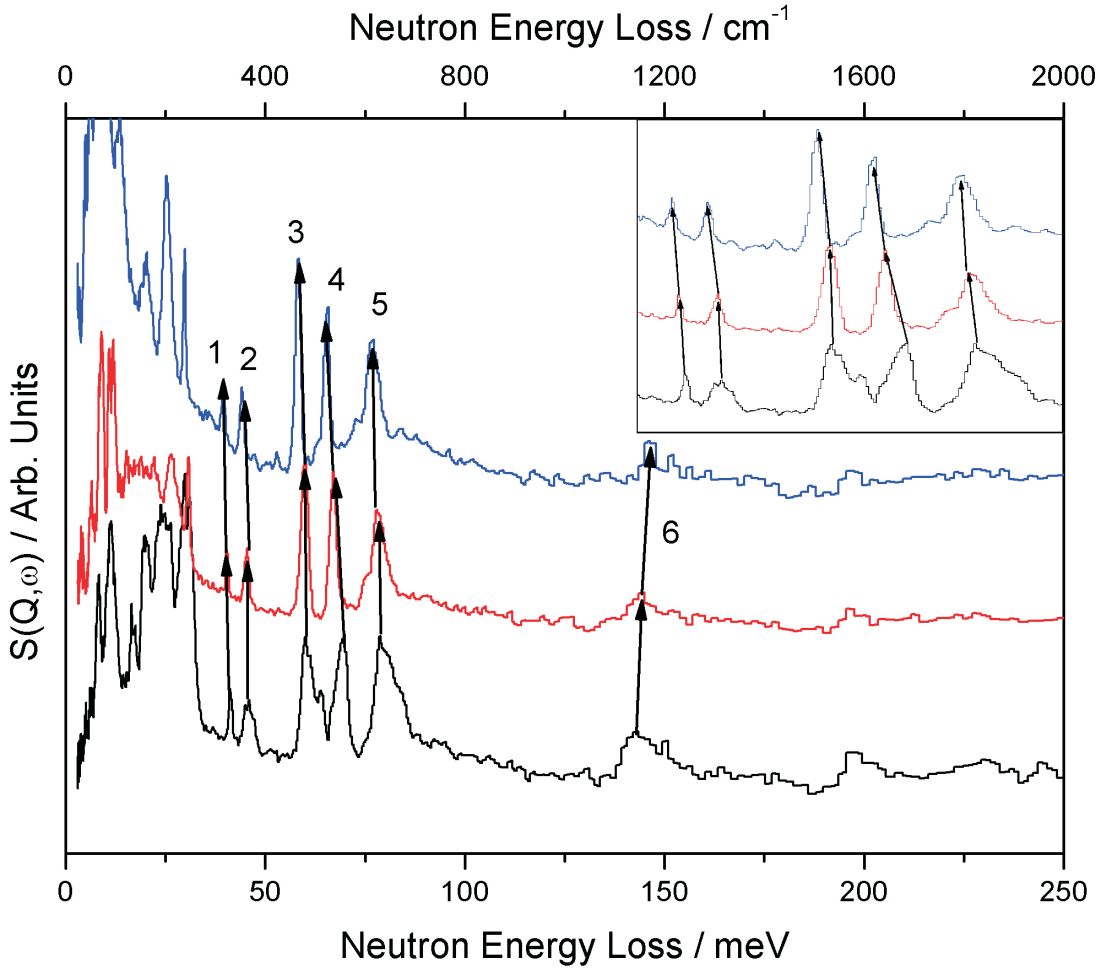

Figure 4.14: The INS spectra of $Mg(NH_3)_6Cl_2$, $Mg(NH_3)_6Br_2$ and $Mg(NH_3)_6I_2$, highlighting the movement of selected modes. The inset shows the spectra between 35 meV and 90 meV.

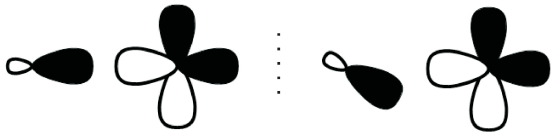

Figure 4.15: A diagrammatic representation of the possible effect of bond angle on σ^* and p-orbital overlap.

4.7 Calculated Structure and Properties

Within disordered systems calculating properties can be hard as electronic calculations require sites of unity occupancy. However, selected calculations may still develop a greater understanding of these systems. Here the site preference of the hydrogen atoms and unknown enthalpies of reaction are investigated.

In order to investigate the preference for different rotational hydrogen sites a series of single point energy calculations were performed that used a completely fixed unit cell with subsequent iterations varying only in the position of 3 hydrogen atoms. The remaining 69 hydrogen atoms were kept constant in the 0 ° position *v.i.*. The 3 moveable hydrogen atoms were rotated clockwise in 5 ° steps between 0 ° defined in Figure 4.16 and 120 ° (the exact equivalent of the 0 ° position).[iii] The results of the calculations are shown in 4.17, and show that there is no clear site preference for the hydrogen atoms. While there are several energy minima, the energy range of 0.000435 eV is small and this suggests that the energy barrier to NH_3 rotation is small and would be equal to thermal energy (kT) at 51 K. Given the use of a simple model, this corroborates well with hydrogen bond driven phase transition observed between 80 and 90 K in the low temperature diffraction data discussed in Section 4.3, it also suggests that the disorder observed at room temperature is dynamic. A more accurate model would need to include rotation of all hydrogen atoms in the cell as their rotation is unlikely to be independent.

Geometry optimisation calculations were performed in an attempt to find the lowest energy ammonia conformations, as an extension of the single point energy calculations discussed above and in order to calculate the enthalpies of formation for the known phases. The structures of $Mg(NH_3)_6X_2$ and $Mg(NH_3)_2X_2$ were optimised using the room temperature structures and positioning all hydrogen atoms in the 0 ° position, calculations converged quickly and the final atomic positions are

[iii] A script enabling this process to be performed is given in Appendix C

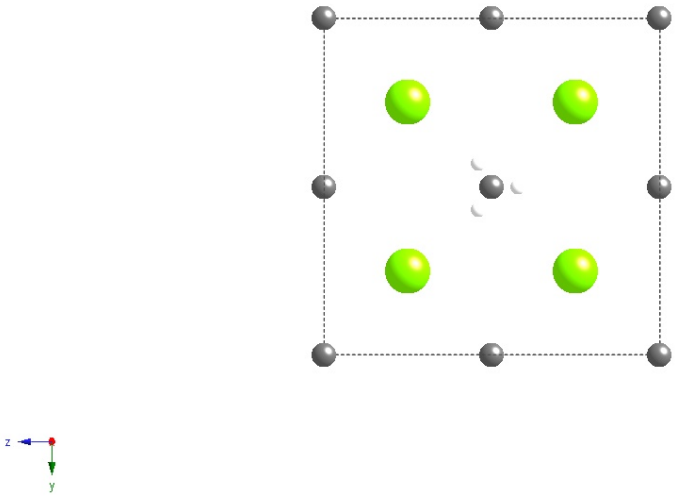

Figure 4.16: A representation of the $Mg(NH_3)_6Cl_2$ model used for DFT single-point energy calculations of different hydrogen sites. All H atoms are hidden other than those that change in subsequent calculations and are shown in the 0 ° position. Magnesium is shown in grey, hydrogen in off white and chlorine in lime green, nitrogen atoms are omitted for clarity.

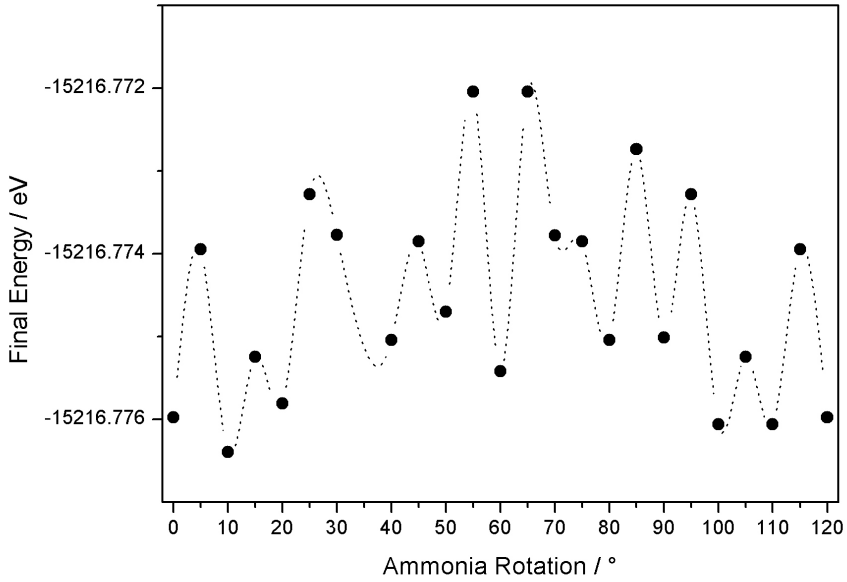

Figure 4.17: The internal energy of $Mg(NH_3)_6Cl_2$ with varying degrees of NH_3 rotation.

given in Appendix E.6 to E.11. The results do not show any rotation of the ammonia molecules, but do show a distortion of the MgN_6 octahedra causing all new structures to belong to the *Cm* space group. Attempts to calculate a structure for $Mg(NH_3)X_2$ beginning with X = Cl and using the atomic coordinates of $Ni(NH_3)Cl_2$ but replacing Ni for Mg and allowing the unit cell to relax were unsuccessful; the iterative calculations failed to converge. This in itself does not suggest that the $Ni(NH_3)Cl_2$ structure is unstable when Ni is replaced with Mg, but is a common problem when attempting to optimise such "soft" systems.

During geometry optimisation calculations the internal energy of the atomic arrangement is calculated, which as discussed in Section 2.12 enables the enthalpy of various reactions to be calculated. Initially the enthalpies of formation were calculated for $MgX_{2\,(s)}$, $Mg(NH_3)_2X_{2\,(s)}$, $Mg(NH_3)_6X_{2\,(s)}$ and $NH_{3\,(g)}$. These are reported in Table 4.6 where a comparison is made to MgX_2 as an assessment of the uncertainty of the calculations. Figure 4.18 confirms the close match between the experimental and calculated enthalpies of formation for MgX_2. The linear fit to the data has a gradient of 1.0(2) and an intercept of 5(1), which suggest a reasonable and consistent uncertainty of 5 $kJmol^{-1}$ in the calculated values compared to the experimental. These uncertainties may arise from errors in the structures used in calculations, in the lack of consideration of any zero-point energy, and in the lack of adjustment from the calculated enthalpy at 0 K and the experimental enthalpy which is not possible given the unknown heat capacities of the phases.

Table 4.6: Calculated and experimental enthalpies of formation of $Mg(NH_3)_nX_2$ given in $kJmol^{-1}$.

	MgX_2		$Mg(NH_3)_2X_2$	$Mg(NH_3)_6X_2$
	Exp.[27]	Calc.	Calc.	Calc.
Cl	-657	-662	-894	-1316
Br	-478	-483	-737	-1182
I	-265	-270	-534	-1015

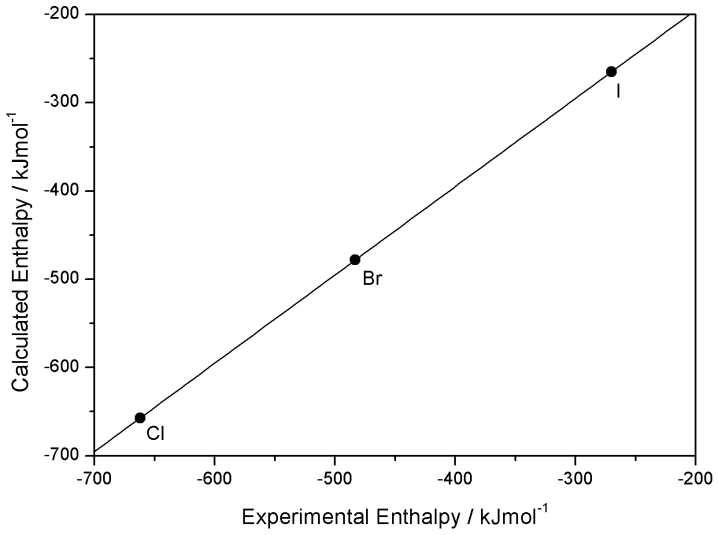

Figure 4.18: A comparison of the calculated and experimental enthalpies of formation of MgX_2.

Using the calculated enthalpies of formation, the enthalpies of reactions 4.1 to 4.3 were calculated. A reasonable agreement to experimental results[iv] for reaction 4.1 and 4.2, is shown in Figure 4.19, the linear fits to the data have gradients of 0.90(9) and 1.2(3), and intercepts of 9(6) and -25(25) for reactions 4.1 and 4.2 respectively. The errors in this case are larger than those in the enthalpy of formation calculations, though this is expected largely due to the compounding of calculative and experimental uncertainty. There is greatest error in the calculation of the enthalpy of reaction 4.2 due to the lack of structural information on $Mg(NH_3)X_2$ meaning that it may not be considered as an intermediate of any reactions, so the enthalpy of the theoretical reaction 4.2 is the best approximation to the real reaction 4.4. The calculated enthalpies of reaction for reaction 4.3 are -94 $kJmol^{-1}$, -105 $kJmol^{-1}$ and -117 $kJmol^{-1}$ for X = Cl, Br and I respectively. These data are discussed further in Section 4.8.1.

[iv] Calculated using Hess's law and the relevant available data.[106]

$$Mg(NH_3)_6X_{2\,(s)} \longrightarrow M(NH_3)_2X_{2\,(s)} + 4\,NH_{3\,(g)} \tag{4.1}$$

$$Mg(NH_3)_2X_{2\,(s)} \longrightarrow MgX_{2\,(s)} + 2\,NH_{3\,(g)} \tag{4.2}$$

$$MgX_{2\,(s)} + 6\,NH_{3\,(g)} \longrightarrow Mg(NH_3)_6X_{2\,(s)} \tag{4.3}$$

$$Mg(NH_3)_2X_{2\,(s)} \longrightarrow Mg(NH_3)X_{2\,(s)} + NH_{3\,(g)} \tag{4.4}$$

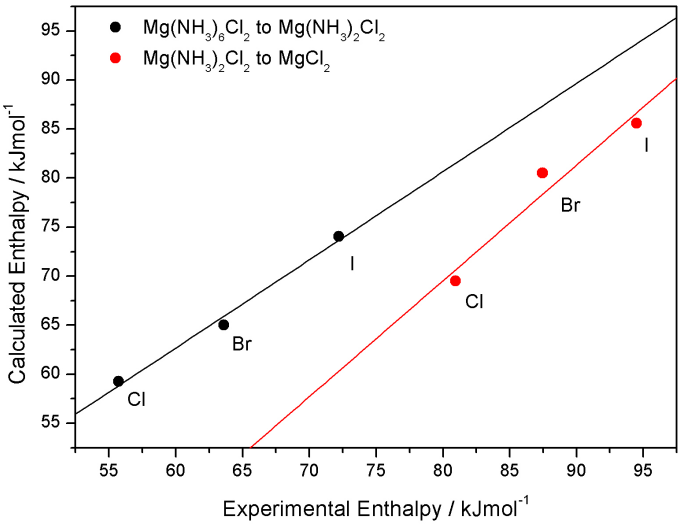

Figure 4.19: A comparison of the experimental and calculated enthalpies of reaction per mole of ammonia for the decomposition of $Mg(NH_3)_6X_2$ to $Mg(NH_3)_2X_2$, and $Mg(NH_3)_2X_2$ to MgX_2. Lines are linear fits to the data, with black and red lines corresponding data of the same colour.

4.8 Conclusions

In this Chapter, a number of trends and similarities have been shown to exist in the magnesium halide ammines. While the most in-depth analysis has been carried out for the chlorides, the similarities of the group suggest that most conclusions may be extended to include the bromides and iodides. Using diffraction techniques, the structures of $Mg(NH_3)_6X_2$ have been confirmed and it has been shown that a dy-

namic ammonia disorder exists down to 90 K in $Mg(NH_3)_6Cl_2$ at which temperature a phase transition occurs. It is likely that weaker hydrogen bonding in the bromide and iodide will result in a lower transition temperature. At room temperature, hydrogen bonding is evidenced through a preference for the 45 ° site that aligns the the N−H with the X^- anion. Simple energy calculations of possible hydrogen sites do not reflect this site preference, but do confirm a low energy barrier to rotation resulting in the low temperature phase transition. The presence of hydrogen bonding has also been confirmed using inelastic neutron spectroscopy for all three halides. Thermogravimetric analysis confirms that each compound decomposes by the 3 step process with the evolution of 4 and sequentially 2 × 1 ammonia molecules, a linear relationship between anion size and decomposition temperature is observed. Both diffraction and NMR confirm that changing the anion has only a small effect on the state of Mg−N bonding. The unknown enthalpies of formation of $Mg(NH_3)_6X_2$ and $Mg(NH_3)_2X_2$ have been calculated, as has the enthalpy of reaction for ammonia adsorption in MgX_2. An increasingly detailed analysis of the presented data follows in Section 4.8.1.

4.8.1 Thermodynamic Consideration of Decomposition

The NMR data and Mg−N bond lengths refined from the powder diffraction data suggest that the anion does not have a significant effect on the state of Mg−N bonding. Given that the desorption temperature increases with increasing anion atomic size, it is sensible to suggest that the overall driving force for loss of ammonia is the negative lattice enthalpy ($U_L[MX_2]$) gained on formation of MgX_2. $U_L[MX_2]$ will naturally be expected to be less favourable for large radius anions. Consequently, where $U_L[MX_2]$ is more favourable (Cl), the temperature for ammonia loss is be expected to be low, and equally where $U_L[MX_2]$ is less favourable the temperature for ammonia loss is be expected to be higher (Br, I). This relationship is summarised in the Hess's law cycle shown in Figure 4.20, and also provides an explanation for the

experimental observation that MgF_2 does not react with ammonia under the same conditions as for X = Cl, Br or I; because of the thermodynamic stability of MgF_2. The calculated enthalpies of ammonia adsorption, that increase in magnitude with increasing anion size, support this theory; as the (MgX_2) lattice energy becomes less favourable the energy gained on NH_3 sorption increases.

If each desorption step is considered individually and an ionic model is assumed, such that each decomposition intermediate is composed of $Mg(NH_3)_n{}^{2+}$ and X^- ions as shown in Figure 4.21, then similar reasoning may be applied: the driving force for each desorption step is the negative lattice enthalpy gained as a result of reducing cation size.

$$\begin{array}{ccc} M(NH_3)_6Cl_{2\,(s)} & \xrightarrow{\Delta H_d} & MgCl_{2\,(s)} + 6\,NH_{3\,(g)} \\ {\scriptstyle U_L[M(NH_3)_6Cl_2]}\uparrow & & \uparrow{\scriptstyle U_L[MCl_2]} \\ M(NH_3)^{2+}_{6(g)} + 2\,Cl^-_{(g)} & \xrightarrow{\Delta H_{d2}} & M^{2+}_{(g)} + 6\,NH_{3\,(g)} + 2\,Cl^-_{(g)} \end{array}$$

Figure 4.20: A Hess's Law cycle for conceptual decomposition of $Mg(NH_3)_6X_2$ directly to MgX_2.

Increasing the size of the anion, X, will lead to a less favourable lattice energy for $M(NH_3)_nX_2$ for all values of n. The contribution of the lattice terms (U_L) to the enthalpy of reaction (ΔH_r, ΔH_{r3} and ΔH_{r5}) will always be negative as $U_L[M(NH_3)_{n+x}X_2]$ must be lower in magnitude than $U_L[M(NH_3)_nX_2]$, (where $x > 0$). Assuming that the enthalpy of ammonia desorption (ΔH_{r2}, ΔH_{r4} and ΔH_{r6}) is approximately constant and independent of anion, as determined by X-ray diffraction and NMR. The negative contribution of $U_L[M(NH_3)_{n+x}X_2]$ and $U_L[M(NH_3)_nX_2]$ to the enthalpy of reaction will decrease proportionally with increasing size of X (as both terms will decrease). Thus, as X increases in size, the enthalpy of ammonia desorption becomes a more significant factor in the overall enthalpy of reaction and the decomposition temperature is observed to increase. The dominance of the cation

size in the lattice energy terms is reflected in the relative enthalpies of formation that are shown in Table 4.7. As the cation increases in size from Mg^{2+} to $Mg(NH_3)_2^{2+}$ and $Mg(NH_3)_6^{2+}$ its radius becomes a more dominant term in determining the lattice energy and as this term is constant for each X the relative stabilities of each phase decrease as the cation size increases.

Table 4.7: Calculated enthalpies of formation of $Mg(NH_3)_nX_2$, and the relative stabilities of Br cf. Cl and I cf. Br for each cation, all values are given in $kJmol^{-1}$.

	MgX_2		$Mg(NH_3)_2X_2$		$Mg(NH_3)_6X_2$	
	Calc.	Rel.	Calc.	Rel.	Calc.	Rel.
Cl	-662	-	-894	-	-1316	-
Br	-483	+179	-737	+157	-1182	+134
I	-270	+213	-534	+203	-1015	+167

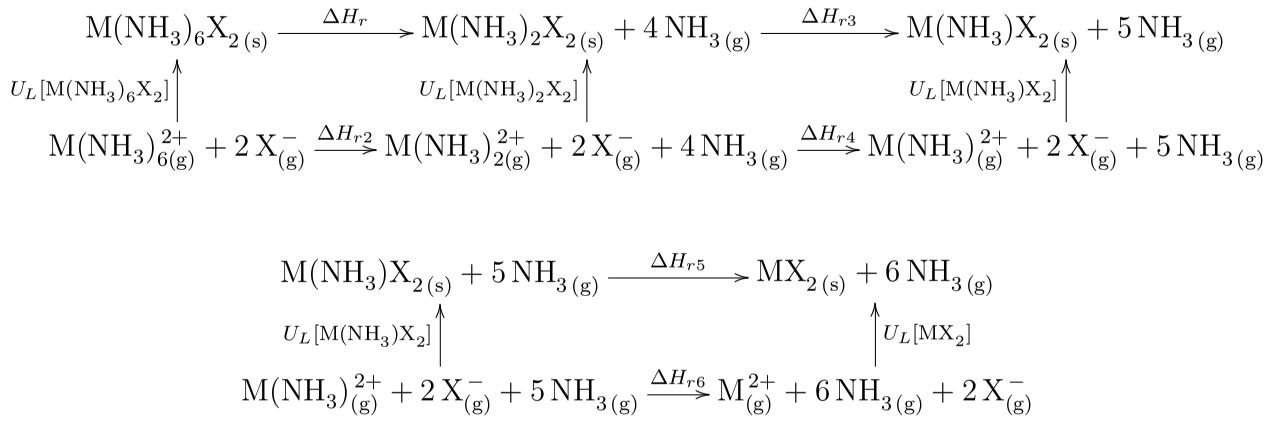

Figure 4.21: A Hess's Law cycle for full decomposition of $Mg(NH_3)_6X_2$ to MgX_2 including the two intermediate steps determined by TGA. Each of the odd numbered steps are the enthalpies of (decomposition) reaction and each of the even numbered steps are the enthalpies of ammonia desorption.

In Section 4.5, Figure 4.11 shows a plot of T_{nP} against ionic radii for the decomposition of $Mg(NH_3)_6X_2$ and reveals a linear relationship between the anionic radii and the peak rate of desorption (T_p) for each of the three steps D_1, D_2 and D_3 at temperatures T_1, T_2 and T_3. The gradients of the lines of best fit are approximately equal for D_2 and D_3 (197 KÅ^{-1}), while that for D_1 is greater (275 KÅ^{-1}). These trends in behaviour may be explained by considering the expression for ΔH_r obtained from Figure 4.21. Assuming an ionic model, it is possible to calculate the lattice enthalpies for $Mg(NH_3)_6X_2$ using the Kapustinskii equation,[107] and assuming that T_{dec} is proportional to ΔH_{dec} the expression for the gradient of the linear fit in Figure 4.11 is obtained in Equations 4.5 to 4.8, where L^+, S^+, and X^- represent large and small cations, and an anion respectively.

$$T_{dec} \propto U_L[LX] - U_L[SX] \tag{4.5}$$

$$T_{dec} \propto \frac{1}{r_{L^+} + r_{X^-}} - \frac{1}{r_{S^+} + r_{X^-}} \tag{4.6}$$

$$T_{dec} \propto \frac{r_{S^+} - r_{L^+}}{(r_{L^+} + r_{X^-})(r_{S^+} + r_{X^-})} \tag{4.7}$$

$$\frac{dT_{dec}}{dr_{X^-}} \propto \frac{(r_{L^+} - r_{S^+})(r_{L^+} + r_{S^+} + 2r_{X^-})}{((r_{L^+} + r_{X^-})(r_{S^+} + r_{X^-}))^2} \tag{4.8}$$

The expression in Equation 4.8 shows that the rate of change of the decomposition temperatures is governed by the change in size of the cation and the anion. As the change in the anion size is constant then the rate of change of T_{dec} with respect to anion radius, $\frac{dT_{dec}}{dr_{X^-}}$, for the first desorption step (D_1) is larger than for the second and third desorption steps (D_2 and D_3) since:

$$r_{Mg(NH_3)_6^{2+}} - r_{Mg(NH_3)_2^{2+}} > r_{Mg(NH_3)_2^{2+}} - r_{Mg(NH_3)^{2+}} \approx r_{Mg(NH_3)^{2+}} - r_{Mg^{2+}}$$

4.8.2 Evaluation as Ammonia Storage Materials

Although the ammonia storage properties of the magnesium halide compounds have been reported in part in other studies, here the group are considered as a whole; decomposition data have been clarified, and ammonia densities and enthalpies of reaction have been determined. The ammonia storage properties of the halides are compared to liquid ammonia in Table 4.8. One of the advantages of using halides as an ammonia store are that they are robust and structural changes or decomposition occur well outside the temperature range required for ammonia sorption, and they allow a lowering of vapour pressure compared to liquid ammonia. A disadvantage is the high temperatures of 100 °C to 180 °C required for release of the first ammonia molecules. With knowledge of the effect changing the anion has on decomposition it is possible, in principle, to tune the decomposition temperature or vapour pressure to the specific requirements of a system or catalyst. A mixed system would also have the potential to produce a constant ammonia pressure over a range of temperatures, avoiding the stepwise lose of ammonia associated with a single halide system.

Table 4.8: Summary of ammonia storage properties of $Mg(NH_3)_6X_2$, compared to liquid NH_3

Compound	Reversible Ammonia Content / wt%	Ammonia Density / gL^{-1}	ΔH_{abs} / $kJmol^{-1}$	Temperature required for complete ammonia release / °C
$Mg(NH_3)_6Cl_2$	52	654	-94	250
$Mg(NH_3)_6Br_2$	36	602	-105	270
$Mg(NH_3)_6I_2$	27	522	-117	330
$NH_{3\,(l)}$ -33°C	100	682	-	-

4.9 Further Work

A large amount of research has already been carried out on these ammines, however a few areas for further work remain. In particular solving the structure of $Mg(NH_3)X_2$ and the low temperature phases would increase the understanding of these compounds. In the case of $Mg(NH_3)X_2$ it should be possible to isolate this phase (in-situ and possibly ex-situ) by heating a sample of $Mg(NH_3)_6X_2$ to the appropriate temperature (T_o) found in Section 4.5. The low temperature phases should exist for all X and it is expected that the transition temperatures would be reduced with increasing anion size. It would also be interesting to investigate the use of mixed anion systems, as this may present the opportunity to tune the decomposition temperature and vapour pressures for desired applications. In terms of applying these materials as commercial ammonia stores, the properties upon cycling must be ascertained, as must methods of dissipating the large ammount of heat produced upon ammonia adsorption.

Chapter 5

Magnesium Borohydride Ammines

5.1 Introduction

Recently the basic structure of $Mg(NH_3)_6(BH_4)_2$ was reported by Soloveichik et al. as part of a paper that focused on the use of $Mg(NH_3)_2(BH_4)_2$ as a promising hydrogen storage material.[51] This Chapter focuses on $Mg(NH_3)_6(BH_4)_2$, its structure and disorder, decomposition pathway and the bonding interactions that explain its properties. Analysis was carried out using X-ray and neutron diffraction, vibrational spectroscopy and thermogravimetric analysis, the data and results are frequently compared to those presented in Chapters 3 and 4 in order to fully understand these materials.

5.2 Room Temperature Diffraction Studies

$Mg(NH_3)_6(BH_4)_2$ has been reported to share the same K_2PtCl_6 structure as the magnesium ammine halides, though reports are not detailed and provide no data on hydrogen positions or disorder. In addition to the inherent NH_3 disorder *v.s.*, the BH_4^- anions may also be disordered. The B atom is positioned on the $\bar{4}3m$ site at $(1/4, 1/4, 1/4)$; when choosing a hydrogen atom position near this site there are

three logical options 1) using the $3m$ site at (x, x, x) that has a a multiplicity of 32; 2) using the m site at (x, x, z) that has a multiplicity of 96; or 3) using both these sites. These three options would produce a BH_4^- anion exhibiting 1-, 3-, or 4- fold disorder respectively. In order to gain a greater understanding of these structural intricacies, both neutron and X-ray diffraction experiments were carried out at room temperature and at variable temperatures from 4 K to 300 K.

5.2.1 X-Ray Powder Diffraction

Samples analysed using X-ray powder diffraction were produced using the method described in Section 2.5 to ammoniate $Mg(BH_4)_2$ purchased from Sigma Aldrich. Room temperature X-ray powder diffraction data were collected using beam line ID31 at the ESRF. The cubic ($Fm\bar{3}m$) K_2PtCl_6 structure was used to model the data using Rietveld refinement, with the same model of ammonia disorder and atomic constraints discussed in Section 4.2. The possible boronic hydrogen atoms were positioned at either (x, x, x) or $(x, x, 0.25)$ using the a B−H bond length that was allowed to vary within the limits of 1.0 Å and 1.4 Å. The final fit to the data, with a GOF (χ) = 1.878 is shown in Figure 5.1, the refined cubic lattice parameter was a = 10.7663(1) Å.

Though it is not appropriate to use these X-ray diffraction data to unambiguously ascertain the level of disorder associated with hydrogen atoms, an improvement in the fit of the model to the data was observed when greater levels of disorder were included. The refined B−H bond length of 1.06(2) Å is shorter than expected, though this may indicate disorder of the BH_4^- anion *v.i.*. The refined Mg−N bond length of 2.161(4) Å is similar to those observed in $Mg(NH_3)_6Cl_2$ and $Mg(NH_3)_6Br_2$, at 2.161(2) Å and 2.167(3) Å respectively. This suggests that any difference in the strength of Mg−N bonding is negligible when changing from a halide to borohydride anion.

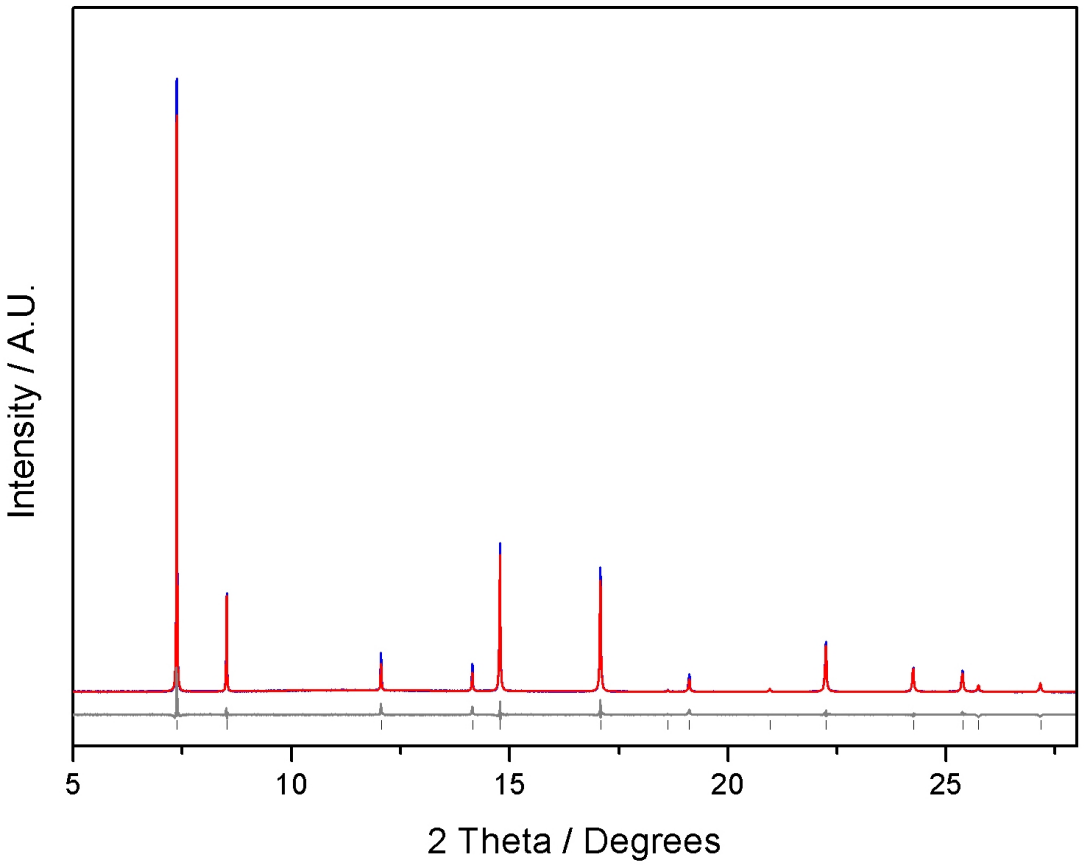

Figure 5.1: Final fit to the data for Rietveld refinement of the $Mg(NH_3)_6(BH_4)_2$ model to X-ray powder diffraction data collected at the ESRF with a wavelength $\lambda = 0.7996$ Å. Experimental data are shown in blue, calculated in red with the difference in grey, tick marks show the expected positions of Bragg reflections.

5.2.2 Neutron Powder Diffraction

Samples analysed using neutron powder diffraction were produced using the method described in Section 2.5 to ammoniate $Mg(^{11}BD_4)_2$ that was produced via the metathesis reaction (described in Section 2.4) between $Na^{11}BD_4$ (synthesised from the elements as described in Section 2.3) and $MgCl_2$ in diethyl ether. Data were collected using GEM and HRPD, but in depth analysis was performed only on data collected using GEM as its high flux lends itself to studying disordered systems, while the high resolution of HRPD is less useful in this case.

Analysis was carried out using the same model as for the X-ray diffraction data and refining it against data collected using GEM banks 2, 3, 4, and 5, the final fit to the data is shown in Figure 5.2. During the refinement process the disorder of the BD_4^- anion was clear, subsequent refinements varying only in the level of BD_4^- disorder showed an improvement in the quality of fit with each added level of disorder. A second indicator of disorder was the refined thermal parameters that were seen to decrease with each added level of disorder. A final indicator was a shorter than expected B−D bond length seen in most ordered model, this suggested a bending or rotating BD_4^- anion meaning the geometric average of deuterium nuclear position was observed. The disordered model allows for this average nuclear positioning so a more realistic B−D bond length of 1.24(2) Å was observed, which agrees strongly with the 1.18(1) Å seen in $Mg(BD_4)_2$.[108]

The refined Mg−N bond length of 2.29(4) Å, is similar to the bond length of 2.272(4) Å seen in $Mg(NH_3)_6Cl_2$ (discussed in Section 4.2.2). According to the X-ray diffraction data discussed in Section 4.2.1, the Mg−N bond length in $Mg(NH_3)_6Br_2$ is slightly longer than in $Mg(NH_3)_6Cl_2$, if this is also the case for $Mg(ND_3)_6Br_2$ then it is expected that the observed $Mg(ND_3)_6(^{11}BD_4)_2$ Mg−N bond lengths are similar to those that would be found in $Mg(ND_3)_6Br_2$. Essentially this means that BD_4^- behaves as a spherical anion in its interaction with ND_3, the presence of the local

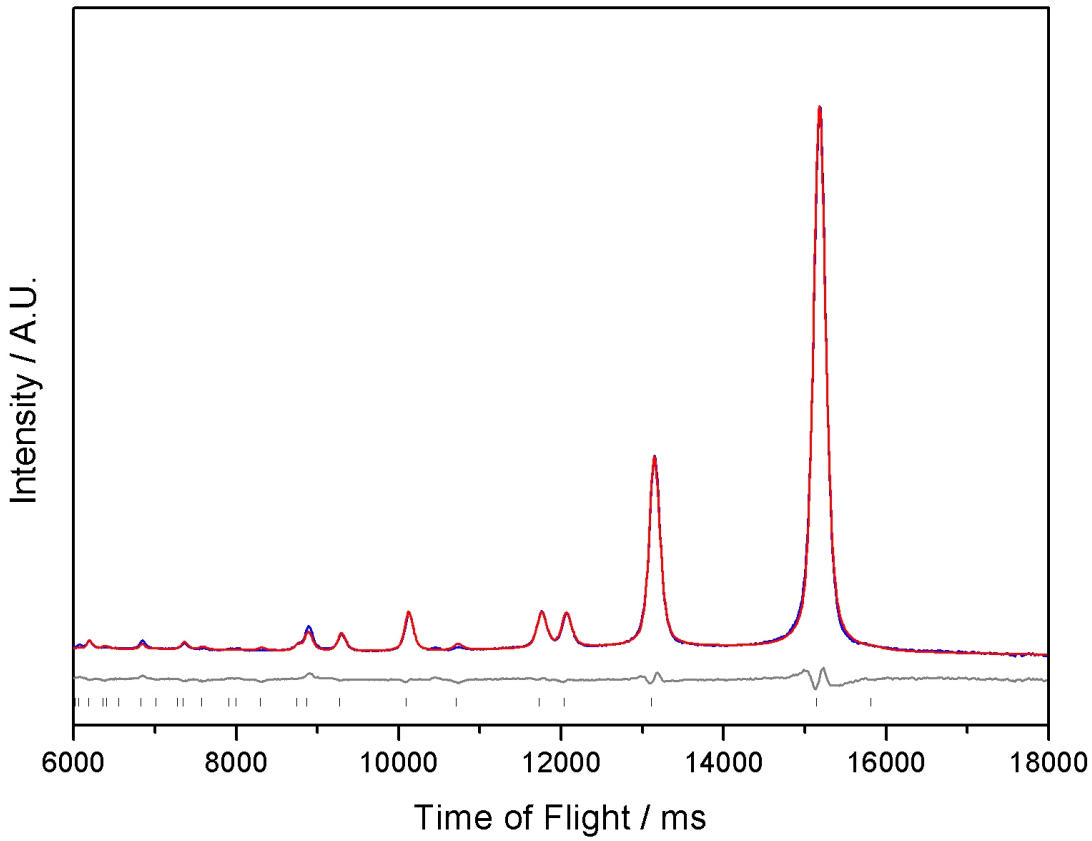

Figure 5.2: Final fit to the data for Rietveld refinement of the $Mg(NH_3)_6(BH_4)_2$ model to neutron powder diffraction data, collected using GEM bank 4 (62 °). Experimental data are shown in blue, calculated in red with the difference in grey, tick marks show the expected positions of Bragg reflections.

B−D polarity and (as discussed in Chapter 4) the anion as a whole has little or no effect on the state of Mg−N bonding.

By allowing the occupancy of the ammonia deuterium sites to vary, the nature of the ND_3 interactions may be established. The refined occupancies of 0.065 0.043 0.102 0.423 for the 0 °, 15 °, 30 ° and 45 ° sites respectively show that there is a strong preference for the 45 ° site. The level of preference is similar, though slightly less well defined than that seen in $Mg(ND_3)_6Cl_2$, this may be because if the disordered BD_4^- anion behaves like a sphere then its lower charge density cf. Cl^- means that any ND···X interactions are weaker and the stabilisation achieved in the 45 ° site is reduced. The minimum ND···DB distances observed were 2.08(2) Å and 1.68(3) Å in the 1-fold and 3-fold disorder models respectively, these distances suggest a dihydrogen bonding interaction. However, there is no evidence here to suggest that this is significantly different from the ND···Cl^- hydrogen bonding observed in $Mg(ND_3)_6Cl_2$ and the other halides.

5.3 Low-temperature Diffraction Studies

The low-temperature phase changes of $Mg(ND_3)_6Cl_2$ were discussed in Section 4.3, given the similarities in structure it is expected that $Mg(NH_3)_6(BH_4)_2$ will also form low-temperature ordered phases. Initial experiments were carried out using beamline ID31 at the ESRF to investigate any low-temperature phases, these experiments were then extended using HRPD at ISIS.

5.3.1 X-ray Powder Diffraction

Initial visual analysis of the X-ray diffraction data shows that three phases exist; the $Fm\bar{3}m$ high temperature (HT) phase, a low temperature (LT) phase and an intermediate (MT) phase. On cooling a gradual transition between the MT and

LT phases was observed to begin at 85 K with the LT phase reflections reaching maximum intensity at 50 K. The LT phase was not isolated and at all temperatures it was observed to coexist with the MT phase. On changing the sample position it was clear that a different phase existed in a nonirradiated section of the sample. This suggests that, as was the case with $Mg(NH_3)_6Cl_2$ (discussed in Section 4.3), the sample was prone to either beam damage or beam heating. The appearance of the high temperature phase at lower temperatures than expected may suggest that hydrogen bonding is an important force in formation of the low temperature phase. The MT phase contains all the Bragg reflections of the HT phase, though with additional reflections of very low intensity. On heating, transition between the MT and HT phase was observed to begin at 238 K with the additional reflections disappearing at 267 K.

5.3.2 Neutron Powder Diffraction

The neutron diffraction data show the same three HT, MT and LT phases as the X-ray data. During this experiment it was possible to cool the sample off-line, employing a slow rate to reach a temperature of 4 K over a period of 24 hours. The result, that at 4K only reflections from the LT phase were observed. The reflections from the LT phase were indexed to a hexagonal unit cell, belonging to the space group $R\bar{3}m$ which as discussed in Section 4.3 is a subgroup of $Fm\bar{3}m$. The lattice parameters of the LT phase at 4K were refined against the data collected using HRPD banks 1, 2 and 3 as a = 15.369(1) Å and c = 34.966(7) with a cell volume of V = 7152(2) Å^3, the final fit to the data is shown in Figure 5.3. The reduced uncertainty compared to the refined $Mg(ND_3)_6Cl_2$ LT unit cell parameters reflects the improvement in the quality of data that was a result of utilising a slow cooling rate.

As seen in the X-ray diffraction data, the MT phase shares all the reflections of

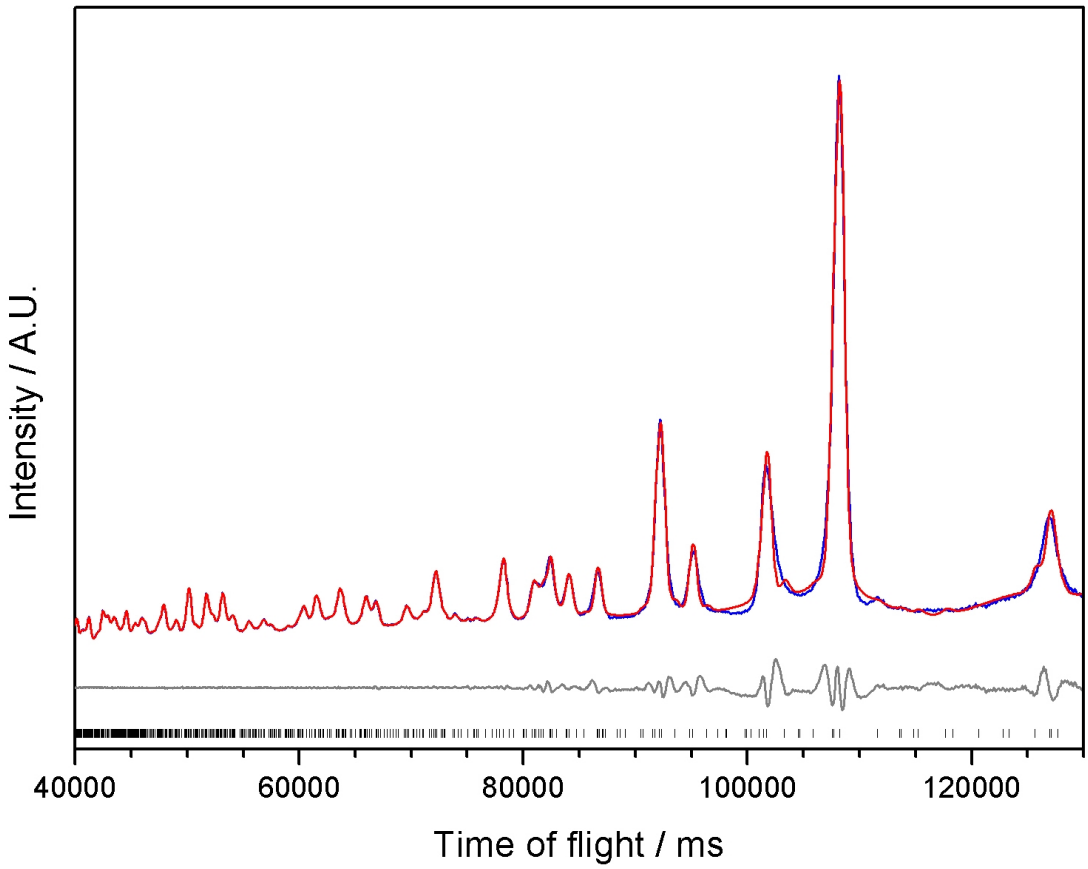

Figure 5.3: The fit to the data for the Pawley refinement of the LT ($R\bar{3}m$) unit cell of $Mg(ND_3)_6(^{11}BD_4)_2$ to the neutron powder diffraction data collected using HRPD bank 2.

the HT ($Fm\bar{3}m$) phase, with several additional reflections of weak intensity. All the reflections of this new phase were indexed in the cubic space group $Fd\bar{3}m$, which was chosen as a subgroup of $Fm\bar{3}m$ that provided the best fit to the data shown in Figure 5.4. The cubic unit cell parameter refined from data collected using HRPD banks 1, 2 and 3 at 150 K is a = 21.2620(2) Å, with a cell volume of V = 9611.9(3) Å^3, thus the MT phase is a $2 \times 2 \times 2$ supercell of the HT phase. It is suggested that as the equivalent cell was not observed in the $Mg(ND_3)_6Cl_2$ data that the transition from the HT to MT phase is a result of ordering of the BD_4^- anions. The similar unit cells of the LT phases of the chloride and borodeuteride suggests that their formation is driven by ND_3 ordering. With such large unit cells and so many H/D atoms, the ideal approach to structure solution would be to position the non-H atoms using X-ray diffraction data. However, the X-ray data are mixed phase so the reliability of the refinements is reduced and the practical difficulty is increased, thus far no attempts at structure solution have been successful.

Phase Transitions

On visual inspection of the neutron diffraction data, it appears that when heating, the transition between the LT and MT phases begins at 95 K and ends when all of the LT phase reflections disappear at 120 K. Transition between the MT and HT phases also occurs over a large range, with the MT reflections reducing in intensity at 200 K and ceasing to appear at 255 K. The change in lattice parameters of the LT phase as a function of temperature is shown in Figure 5.5, with the equivalent plot for the volume shown in Figure 5.6. These Figures show that a first order phase transition occurs between 60 K and 70 K, but that both phases either have the same space group, or that one phase is in a subgroup of the other. It is possible that the lower temperature phase belongs to the lower symmetry $R\bar{3}$ space group that was predicted to contain the LT structure of $Mg(NH_3)_6Cl_2$,[44] and in this case is not distinguishable from $R\bar{3}m$ using Pawley refinement. The data for the LT phase of

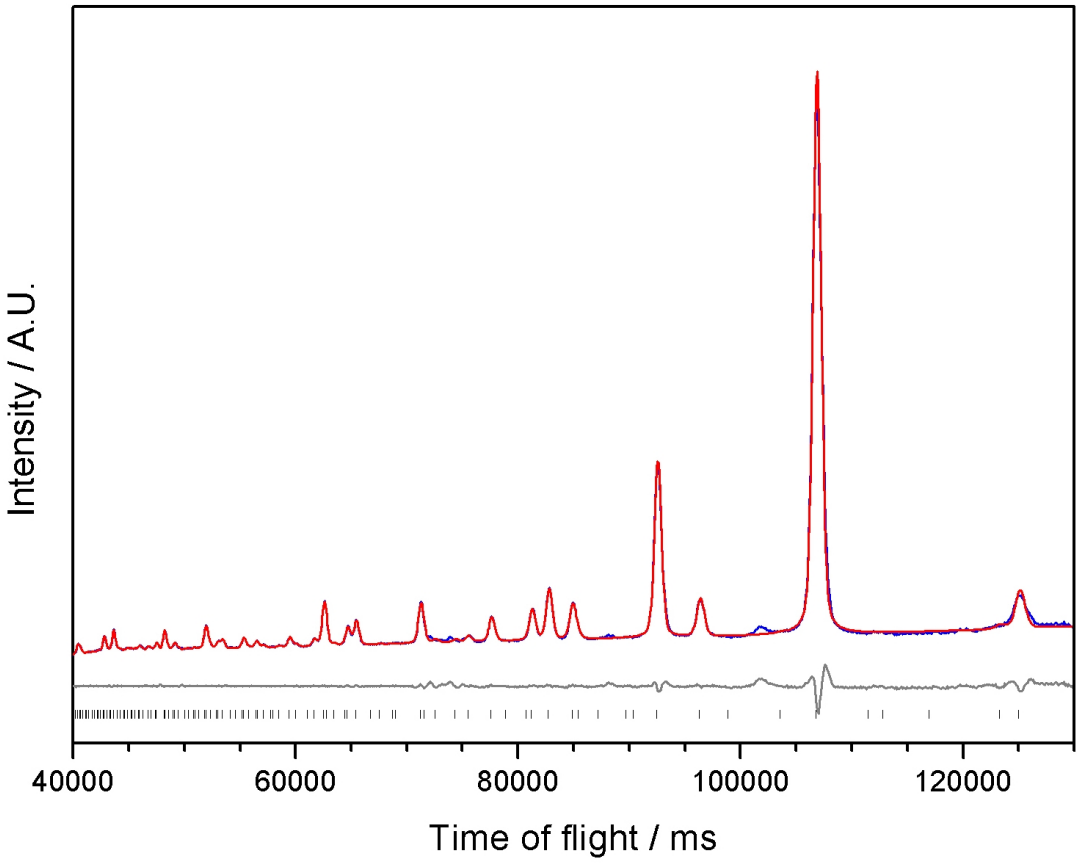

Figure 5.4: The fit to the data for the Pawley refinement of the MT ($Fd\bar{3}m$) unit cell of $Mg(ND_3)_6(^{11}BD_4)_2$ to the neutron powder diffraction data collected using HRPD bank 2.

$Mg(ND_3)_6Cl_2$ do not show any similar phase transition. The transition between the LT and MT phases of $Mg(NH_3)_6(BH_4)_2$ occurs at higher temperature than the LT to HT phase transition of $Mg(NH_3)_6Cl_2$, this implies that weaker hydrogen bonding exists in $Mg(NH_3)_6(BH_4)_2$ and that BH_4^- still behaves as a spherical anion even in the low temperature phases. The potential NH···HB interactions are not significant compared to the overall NH···BH_4^- interactions.

The transition between the MT and HT phases can be followed by observing the intensity of the (731) reflection (I_{731}), as shown in Figure 5.7. The plot of I_{731} shows that a gradual phase transition occurs between approximately 140 K and 260 K, and that the I_{731}^3 shows an almost linear variation in response to temperature in this range. The lattice parameters shown in Figure 5.8 show more clearly that the transition is second order and occurs between 160 K and 260 K, with two distinct rates of change seen for the HT and MT lattices confirming that there is a difference in the chemistry and behaviour of the two phases.

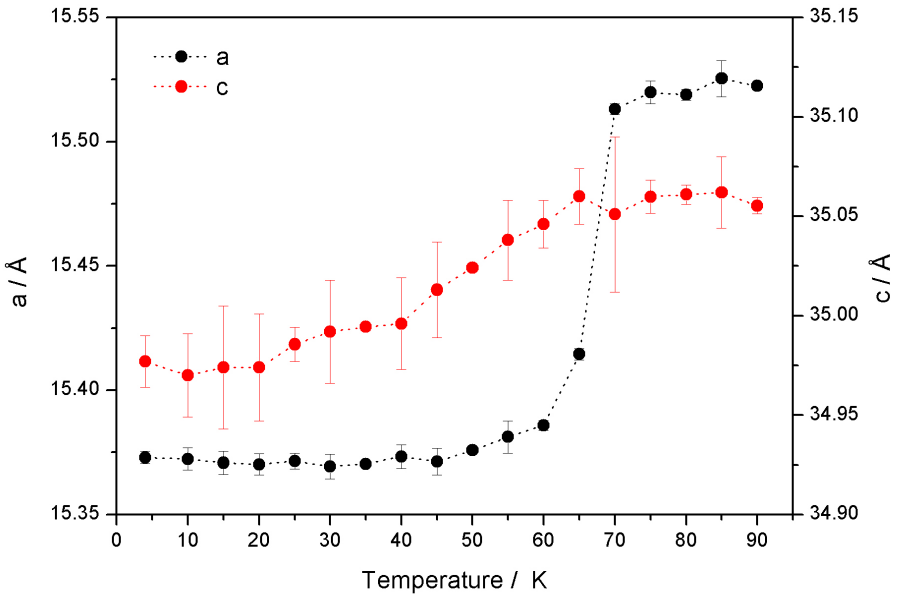

Figure 5.5: The lattice parameters of the LT phase of $Mg(ND_3)_6(^{11}BD_4)_2$ as a function of temperature.

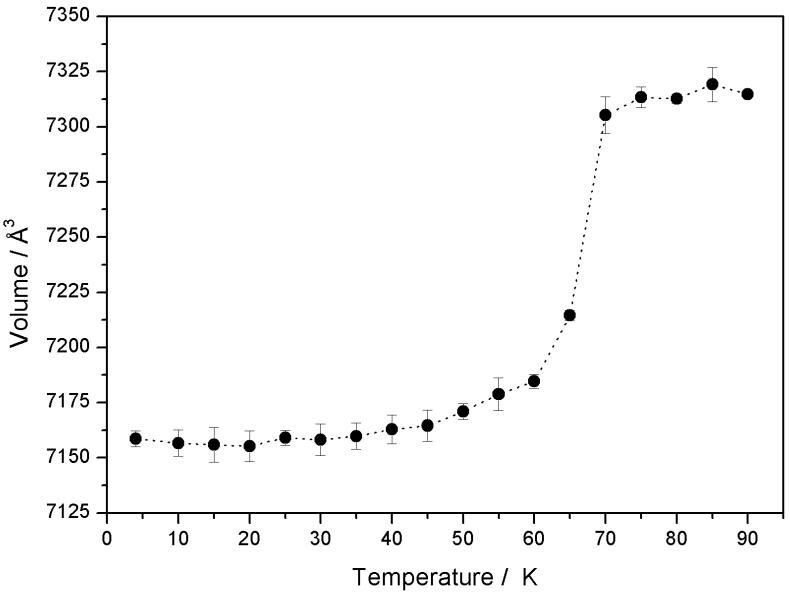

Figure 5.6: The volume of the LT phase of $Mg(ND_3)_6(^{11}BD_4)_2$ as a function of temperature.

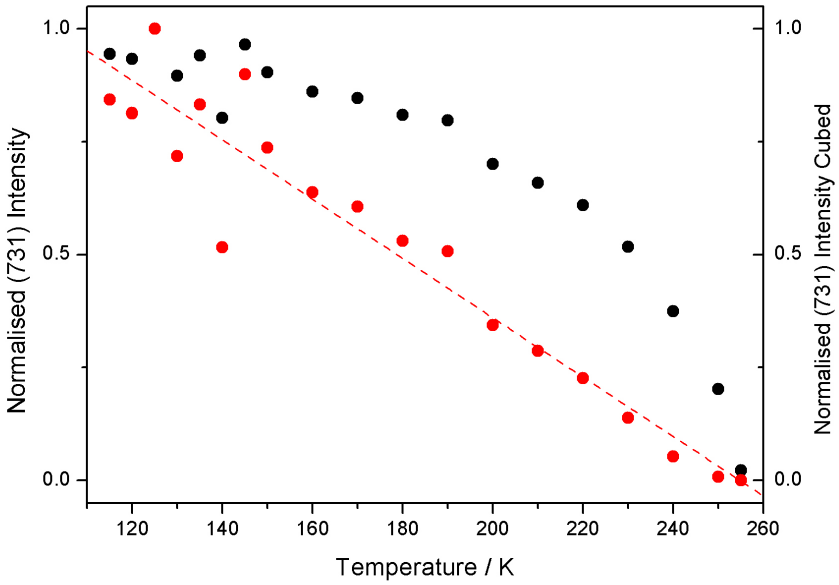

Figure 5.7: The intensity of the (731) reflection (I_{731}) of the MT phase of $Mg(ND_3)_6(^{11}BD_4)_2$ in black and $I^3_{(731)}$ in red as a function of temperature, the dashed line indicates a linear fit to all $I^3_{(731)}$ data.

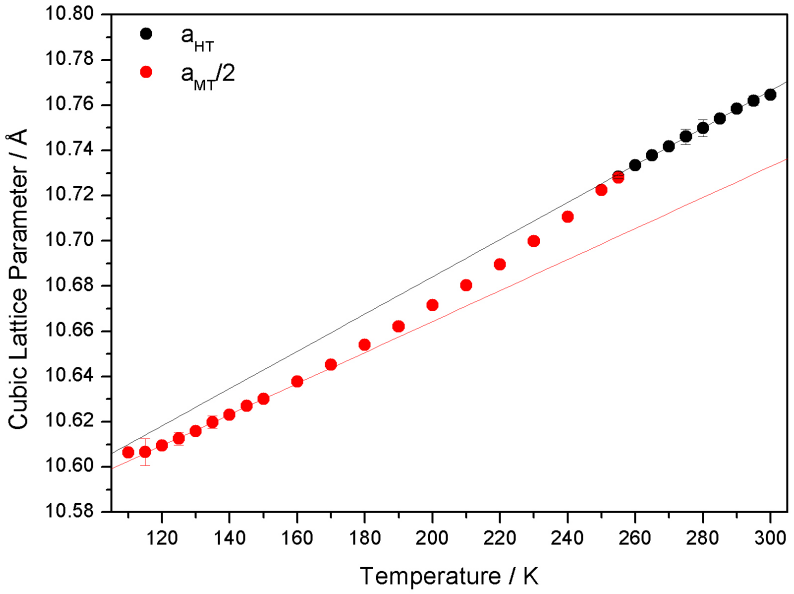

Figure 5.8: The lattice parameters of the HT (a_{HT}) and MT/2 ($a_{MT}/2$) phases of $Mg(ND_3)_6(^{11}BD_4)_2$ as a function of temperature.

5.4 Raman Spectroscopy

The Raman spectra of $Mg(NH_3)_6(BH_4)_2$ is shown in Figure 5.9, where the similar spectra of $Li(NH_3)BH_4$ that is discussed in detail in Section 3.3.6 is also shown for comparison. The principle mode in the BH_4^- region appears at the same wavenumber in both spectra, confirming the existence of discrete BH_4^- anions in both materials. The lower intensity of the side bands in the BH_4^- stretching region of the $Mg(NH_3)_6(BH_4)_2$ spectra may suggest that the anion here is in a higher symmetry environment than in $Li(NH_3)BH_4$, this is consistent with the disorder seen in the diffraction data. The shape of the NH_3 stretching bands is highly similar in both spectra, the most intense line is seen at a frequency of 3267 cm^{-1} in $Mg(NH_3)_6(BH_4)_2$ compared to 3296 cm^{-1} in $Li(NH_3)BH_4$. This suggests a weakening of the N−H bond in the magnesium compound, most likely caused by stronger M−N bonding rather than NH···BH_4^- interactions. In the spectra of $LiBH_4$, a mode that was not calculated was observed at 3172 cm^{-1} and was attributed to vibration rotation coupling between NH_3 stretches and NH_3 rotations. This mode is also observed in $Mg(NH_3)_6(BH_4)_2$ and in this case the spacing between the main mode and the additional mode is 124 cm^{-1}. This is compared to an observed spacing of 81 cm^{-1} in the $Li(NH_3)BH_4$ spectra, and suggests that the NH_3 rotational modes appear at higher energies in $Mg(NH_3)_6(BH_4)_2$. The increased barrier to rotation and stronger NH···BH_4^- interactions are attributed to the local (albeit weak) interaction with 4 nearest neighbour anions per ammonia molecule in $Mg(NH_3)_6(BH_4)_2$ compared to the local interaction with just one anion seen in $Li(NH_3)BH_4$.

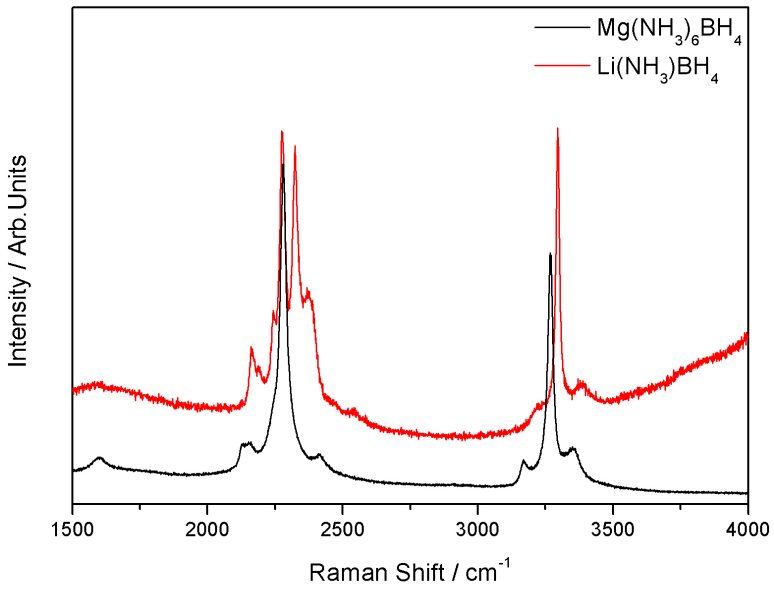

Figure 5.9: The Raman spectra of $Mg(NH_3)_6(BH_4)_2$ in black and $Li(NH_3)BH_4$ in red.

5.5 Inelastic Neutron Spectroscopy

INS data for a sample of $Mg(NH_3)_6(BH_4)_2$ (with all elements at their natural isotopic abundance) were collected using TOSCA at 20 K, the resulting Spectra is shown in Figure 5.10. The similarities to spectra of the $Mg(NH_3)_6X_2$ halides are clear and this reflects the structural similarities of the group. For ease of comparison the relative positions of common NH_3 libration, rocking and umbrella modes (discussed in detail in Section 4.6) are highlighted by dashed lines, and it is clear that the modes for the borohydride sit at an intermediate position between bromide and iodide. This suggests that the trends follow the size of the anion; the hydrogen atoms present in BH_4^- do not effect the movement of the NH_3 molecules and the charge density of the BH_4^- anion is the most important factor. It is proposed that this is because the orientation of the BH_4^- unit in the high temperature phase does not allow for directional dihydrogen bonding to all NH_3 molecules. The phase present during the measurements is likely to have frozen BH_4^- disorder, thus the average hydrogen atom position produces a spherical ion of radius 2.05 Å.

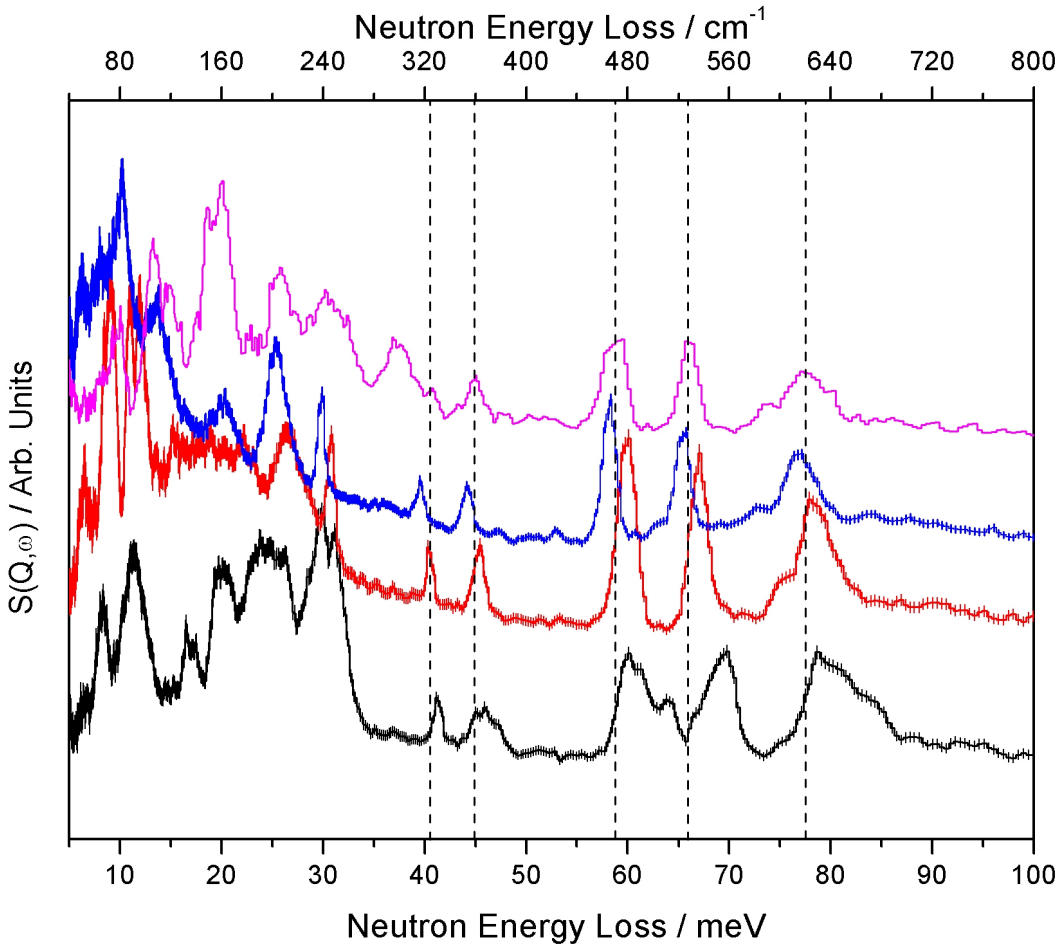

Figure 5.10: The INS spectra of $Mg(NH_3)_6X_2$ with X = BH_4, I, Br and Cl shown in pink/purple, blue, red and black respectively. Positions of particular modes in $Mg(NH_3)_6(BH_4)_2$ are indicated by dashed lines.

5.6 Gravimetric Analysis

Gravimetric analysis was carried out using the TGA, RGA, and IGA equipment detailed in Chapter 2. The use of a variety of techniques allows for a thorough analysis of decomposition, that is necessary both for comparison with other data presented in this Thesis and to clarify the contradicting reports in the literature.[50,51]

5.6.1 Thermogravimetric Analysis (TGA)

Thermogravimetric, TGA, analysis of $Mg(NH_3)_6(BH_4)_2$ was carried out using the procedure described in Section 2.11.1. Measurements were carried out using a heating rate of 2 °Cmin^{-1} under a 1 bar argon atmosphere with a flow rate of 5 mlmin^{-1}. Data are shown in Figure 5.11, where it can be seen from the plot of $(\frac{dm}{dt})$ that up to 575 °C there are four mass loss steps with T_{p1} = 144 °C, T_{p2} = 200 °C, T_{p3} = 226 °C and T_{p4} = 427 °C. No plateaus distinguishing between steps one, two and three are observed meaning that it is hard to assign the intermediates, though T_{p2} matches the 200 °C reported for $Mg(NH_3)_2(BH_4)_2$, suggesting this phase has formed after the first step and then decomposed. The subsequent two-step decomposition of $Mg(NH_3)_2(BH_4)_2$ below 400 °C is also consistent with reported data.[51]

It is assumed, that the lowest mass reached corresponds to complete hydrogen loss and an empirical formula of MgB_2N_2. The fourth mass loss at at T_{p4} = 427 °C is close to the decomposition temperature of MgH_2,[109] and if this is present or not an empirical formula of $MgB_2N_2H_2$ is consistent with the first plateau product. Taking the mean molar amount of sample from these two points gives a starting sample of $Mg(NH_3)_{5.4}(BH_4)_2$, that is to say either the starting ammine was produced with 90 % yield or some ammonia was lost from the sample on evacuation of the sample vessel during synthesis. The masses of these assumed products are shown in Figure 5.11. Overall, the analysis shows that decomposition occurs according to Reactions 5.1 and 5.2, the small amount of sample available after the

TGA experiment meant that no additional data to help identify the decomposition products could be obtained.

$$Mg(NH_3)_6(BH_4)_2 \longrightarrow Mg(NH_3)_2(BH_4)_2 + 4\,NH_3 \tag{5.1}$$

$$Mg(NH_3)_2(BH_4)_2 \longrightarrow X \longrightarrow MgB_2N_2H_2 \longrightarrow MgB_2N_2 \tag{5.2}$$

The first mass loss step has an onset of T_o = 105 °C, this is lower than the equivalent bromide or iodide, but higher than the chloride. The evidence in the diffraction and vibrational spectroscopy data suggests that the disordered BH_4^- acts as a spherical anion. Considering the argument for decomposition of $Mg(NH_3)_6X_2$ based on an ionic model presented in Section 4.8.1 and shown for $Mg(NH_3)_6(BH_4)_2$ in Figure 5.12; $Mg(NH_3)_6(BH_4)_2$ should decompose at a temperature close to the halide with the most similar anionic radii, $Mg(NH_3)_6Br_2$ (2.03 Å for BH_4^- cf. 1.96 Å for Br^-).[105,110] The lower than expected T_1 shows that in this case the purely ionic model is no longer appropriate and its breakdown may be explained by the presence of dihydrogen bonding that acts to stabilise the intermediate $Mg(NH_3)_2(BH_4)_2$ but not the starting $Mg(NH_3)_6(BH_4)_2$, the presence of such bonding was proposed by Soloveichik et. al..[51]

5.6.2 Residual Gas Analysis (RGA)

The decomposition products were investigated using RGA, with measurements carried out at Birmingham University. A sample of $Mg(NH_3)_6(BH_4)_2$ was heated at a rate of 3 °Cmin^{-1} with the output gas scanned for the presence of matter with masses between 1 and 50 a.m.u. The strong signals that were detected for NH_3 and H_2 and are shown in Figure 5.13. The two stages of gas release that are observed fit with the TGA data and are consistent with the decomposition pathway shown in Reactions 5.1 and 5.2. The multiple maxima of the H_2 plot suggest that there

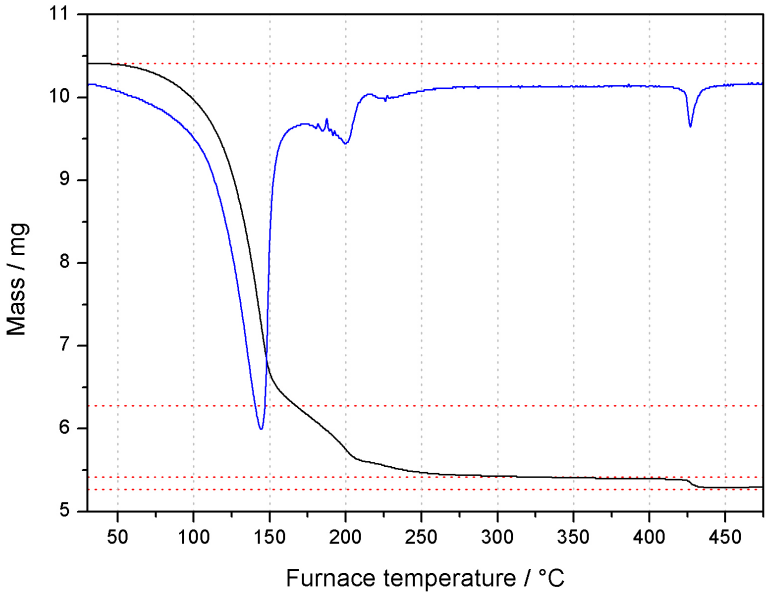

Figure 5.11: Mass loss as a function of temperature for $Mg(NH_3)_6(BH_4)_2$ in black, with the first derivative of the mass with respect to time ($\frac{dm}{dt}$) in blue. Red dotted lines indicate masses corresponding to (from top to bottom) $Mg(NH_3)_{5.4}(BH_4)_2$, $Mg(NH_3)_2(BH_4)_2$, $MgN_2B_2H_2$ and MgN_2B_2.

$$\begin{array}{ccc} \mathrm{Mg(NH_3)_6(BH_4)_{2\,(s)}} & \xrightarrow{\Delta H_r} & \mathrm{Mg(NH_3)_2(BH_4)_{2\,(s)} + 4\,NH_{3\,(g)}} \\ {\scriptstyle U_L[\mathrm{Mg(NH_3)_6(BH_4)_2}]}\uparrow & & \uparrow{\scriptstyle U_L[\mathrm{Mg(NH_3)_2(BH_4)_2}]} \\ \mathrm{Mg(NH_3)^{2+}_{6(g)} + 2\,BH^-_{4(g)}} & \xrightarrow{\Delta H_{r2}} & \mathrm{Mg^{2+}_{(g)} + 6\,NH_{3\,(g)} + 2\,BH^-_{4(g)}} \end{array}$$

Figure 5.12: Hess's Law cycle for decomposition of $Mg(NH_3)_6(BH_4)_2$ to $Mg(NH_3)_2(BH_4)_2$.

are several intermediates associated with the decomposition that leads to hydrogen release.

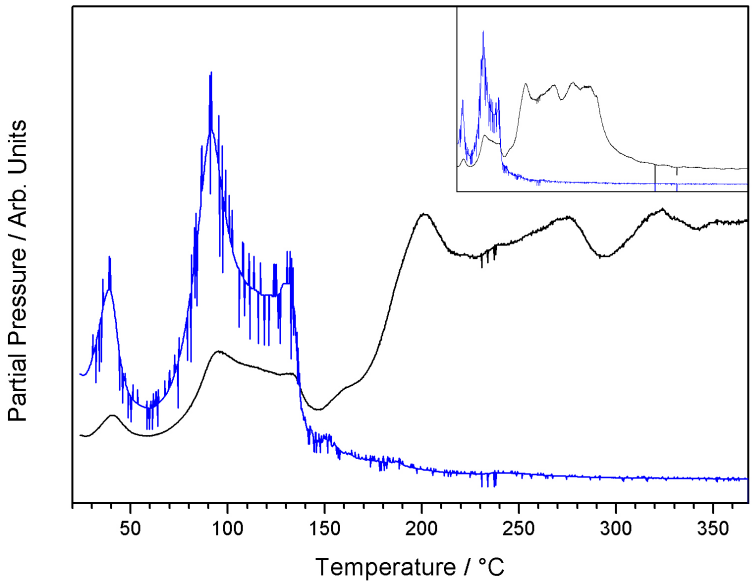

Figure 5.13: The partial pressures of NH_3 in blue and H_2 in black produced during heating of $Mg(NH_3)_6(BH_4)_2$.

5.6.3 Intelligent Gravimetric Analysis (IGA^n)

In order to assess the stability of $Mg(NH_3)_2(BH_4)_2$ and to establish the potential suitability of $Mg(NH_3)_6(BH_4)_2$ as an ammonia storage material, a cycling experiment was carried out using the IGA^n equipment with and without neutron diffraction. The data collected without neutron diffraction are shown in Figure 5.14. Here it can be seen that at a constant temperature of 75 °C it was possible to convert between the $Mg(NH_3)_6(BH_4)_2$ and $Mg(NH_3)_2(BH_4)_2$ by changing the pressure between 250 mbar of ammonia and the 'outgas' mode of the IGA^n (nominally 0 bar).

Attempts to perform this experiment in-situ whilst collecting neutron diffraction data were of limited added value. It was found that the Bragg reflections for $Mg(ND_3)_6(^{11}BD_4)_2$ decreased in intensity as ammonia loss occurred. The mass

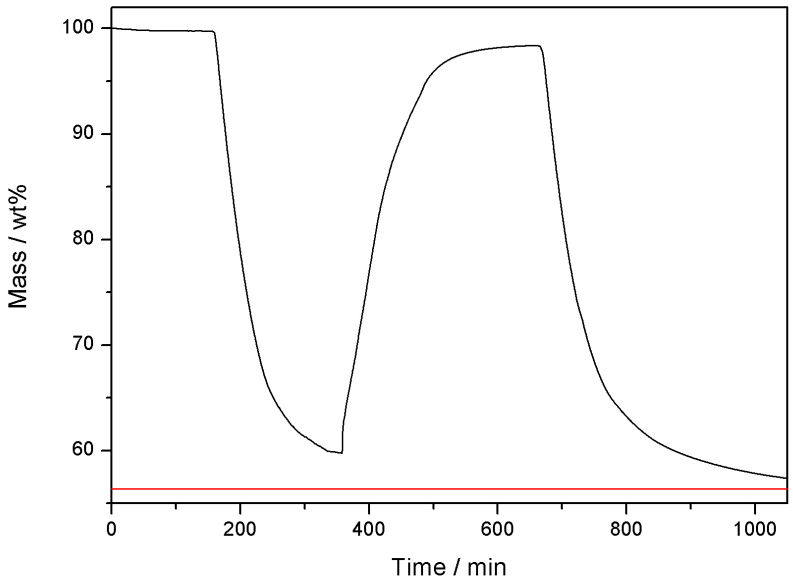

Figure 5.14: Mass as a function of time for $Mg(NH_3)_6(BH_4)_2$, data were collected cycling between an ammonia pressure of 250 mbar and 'outgas' at a temperature of 75 °C. The red line corresponds to complete conversion to $Mg(NH_3)_2(BH_4)_2$ assuming a starting sample of 100 % $Mg(NH_3)_6(BH_4)_2$.

trace showed a lumpiness that is characteristic of a gas loss from a liquid with a solid crust, it is proposed that at this temperature $Mg(ND_2)_2(^{11}BD_4)_2$ is a liquid and thus did not produce Bragg reflections. Attempts to cool the sample resulted in the appearance of some reflections, though with a poor signal to noise ratio, such that no useful data were gained for further analysis.

5.7 Conclusions

In this Chapter it has been shown that the properties of $Mg(NH_3)_6(BH_4)_2$, including its vibrational spectra, its initial decomposition and the size of its unit cell, may all be explained by considering it as part of the $Mg(NH_3)_6X_2$ series where the anion BH_4^- sits between Br^- and I^-. The nature of disorder within $Mg(NH_3)_6(BH_4)_2$ has been established using a variety of techniques, at room temperature the BH_4^- anion exhibits a fourfold disorder which is why it behaves in an analogous manner to the halides. The similarity with the halides is further reflected in the similar Mg−N bond lengths and favoured occupancy of the 45 ° NH_3 hydrogen site. The additional B−H bonds are irrelevant until it comes to the formation of $Mg(NH_3)_2(BH_4)_2$, where the formation of dihydrogen bonds allow significant stabilisation of the diammine compared to the equivalent halides.

5.7.1 Evaluation as Ammonia Storage Material

It has been shown that it is possible to reversibly cycle between the hexa- and di-ammines, though the potential for irreversible decomposition of the diammine may limit the effective lifetime of the material. The storage properties are compared to $Mg(NH_3)_6Cl_2$ in Table 5.1, where it can be seen that the useful ammonia content of $Mg(NH_3)_6(BH_4)_2$ is reduced as a result of the irreversible decomposition of the diammine. The advantage of the using the borohydride over the chloride is the low

and constant temperature required for complete ammonia release. The conclusion that a stabilised intermediate may help to lower the desorption temperature of ammines may be used in attempts to design ammonia storage materials with lower decomposition temperatures.

Table 5.1: Summary of ammonia storage properties of $Mg(NH_3)_6(BH_4)_2$, compared to $Mg(NH_3)_6Cl_2$ and liquid NH_3.

Compound	Reversible Ammonia Content / wt%	Ammonia Density / gL^{-1}	Temperature required for complete ammonia release / °C
$Mg(NH_3)_6Cl_2$	52	654	250
$Mg(NH_3)_6(BH_4)_2$	50	543	75
$NH_{3\,(l)}$ -33°C	100	682	-

5.7.2 Further Work

The use of $Mg(NH_3)_6(BH_4)_2$ as an ammonia store may be limited given the instability of $Mg(NH_3)_2(BH_4)_2$ around the temperatures that ammonia is released from the hexa-ammine, however a number of interesting areas for further work remain. In particular determining the decomposition products formed using in-situ ^{25}Mg and ^{11}B NMR, diffraction and possibly pair distribution function (PDF) analysis would be useful in determining the potential reversibility of the decomposition and the suitability of $Mg(NH_3)_2(BH_4)_2$ as a hydrogen storage material. The hydrogen storage properties of $Mg(NH_3)_2(BH_4)_2$ have only been discussed briefly but is a material with huge potential. Solving the low temperature structures would increase the general understanding of this material and provide an interesting crystallographic study. A potential use for the borohydride anion in ammonia storage materials may be in producing mixed anion systems with bromine or chlorine, wherein the borohydride may act to stabilise intermediates and reduce decomposition temperatures.

Chapter 6

Conclusions and Further Work

In this Thesis, $Li(NH_3)_nBH_4$ and $Mg(NH_3)_nX_2$ (with X = Cl, Br, I and BH_4) have been investigated as potential ammonia storage materials. Detailed conclusions are discussed at the end of Chapters 3 to 5, but a brief summary and some common features are presented here. In this Chapter, the potential use as ammonia storage materials is concluded and discussed. This is followed by a summary of the points of more general interest and some final conclusions.

As reported in Chapter 1, $Mg(NH_3)_6Cl_2$ has been proposed as a promising ammonia storage material,[18] with the primary benefit of having a high ammonia density of 654 gl^{-1} and a low vapour pressure. This ammonia density is higher than the novel materials investigated in this Thesis, with $Li(NH_3)_4BH_4$ at 539 gl^{-1} and $Mg(NH_3)_6(BH_4)_2$ at 543 gl^{-1}. Moreover, $Mg(NH_3)_6(BH_4)_2$ falls short in its gravimetric ammonia density, containing only 50 wt% of recoverable ammonia compared to $Mg(NH_3)_6Cl_2$ with 52 wt%, $Li(NH_3)_4BH_4$ excels in this respect as it contains 76 wt% ammonia. The borohydride compounds succeed in lowering the energy exchange associated with ammonia cycling, as they require temperatures of 50 °C and 75 °C respectively to release all adsorbed ammonia, compared to 250 °C for the chloride system. These comparisons are assuming a desorption method that involves elevated temperatures (in the style of TGA), but a key benefit of using

$Li(NH_3)BH_4$ is that, as reaction 6.1 shows, it allows storage of 57 wt% ammonia using the room temperature pressure swing absorption (PSA) method operating between ca. 24 mbar and 110 mbar. This compares favourably to the leading PSA candidate $Ca(NH_3)_8Cl_2$, that can be used to store 41 wt% ammonia using PSA between 700 mbar and 2.1 mbar as shown in Reaction 6.2.[25] Some key ammonia storage data collated from Chapters 3, 4 and 5 are given in Table 6.1.

$$Li(NH_3)_4BH_4 \longrightarrow Li(NH_3)BH_4 + 3\,NH_3 \tag{6.1}$$

$$Ca(NH_3)_8Cl_2 \longrightarrow Ca(NH_3)_2Cl_2 + 6\,NH_3 \tag{6.2}$$

Table 6.1: A summary of the ammonia storage properties of materials investigated in this Thesis in comparison to liquid ammonia

Compound	Reversible Ammonia Content / wt%	Ammonia Density / gl^{-1}	Vapour Pressure at 25 °C / mbar	Temperature required for complete ammonia release / °C
$Li(NH_3)BH_4$	41	296	6.7	50
$Li(NH_3)_2BH_4$	61	385	24	50
$Li(NH_3)_3BH_4$	70	526	96	50
$Li(NH_3)_4BH_4$	76	539	110	50
$Mg(NH_3)_6Cl_2$	52	654	1.97[25]	250
$Mg(NH_3)_6Br_2$	36	602	-	270
$Mg(NH_3)_6I_2$	27	522	-	330
$Mg(NH_3)_6(BH_4)_2$	50	543	-	75
$NH_{3\,(l)}$ -33°C	100	682	1017	-

In terms of developing these materials as viable, large scale, ammonia stores, careful though must be given the final application. The borohydrides may produce good lightweight storage materials but they suffer from relatively facile decomposition, which means that theses systems are less robust than those based on halides which have substantially higher melting points and decomposition temperatures. The choice of starting material must depend on the end-use application. There may be requirement to operate at specific temperatures or pressures and withstand more

aggressive heating or loading regimes in an 'industrial' environment compared to the laboratory.

Considering future research, the next step for each system must be to perform cycling experiments to determine any loss of capacity on repeated cycles. It would also be necessary to determine the effect of pelletisation and use of bulk samples on storage properties. A key consideration will be the heat of absorption; this was calculated (in Chapter 4) to range between -91 $kJmol^{-1}$ and -117 $kJmol^{-1}$ for the magnesium halides. It would be useful for these to be experimentally determined in order to assess the thermal conductivity requirements of any large scale system. Investigating pressure-composition relationships at elevated and fixed temperatures, in a method similar to the $Mg(NH_3)_6(BH_4)$ 75 °C cycling experiments, would also be beneficial as varying just the temperature or the pressure will create the simplest system in terms of engineering and manufacture. An interesting investigation would involve determining if mixes of anions allow steady ammonia release over a temperature range, or even allow a combination of the seemingly exclusive properties of low vapour pressure and low temperature desorption. For example, in an ammine consisting of $MgCl_2$ and MgI_2, the chloride would release ammonia at lower temperatures while the iodide would absorp at low vapour pressures.

Besides the ammonia storage capacity of these materials, they have provided a number of interesting results. Discussion presented throughout this Thesis concludes that disorder is present in all these ammines and is primarily associated with rotating ammonia molecules. The nature of the disorder has proved a determining factor in the material properties, for example in $Mg(NH_3)_6(BH_4)_2$ the BH_4^- anion is disordered and behaves analogously to the halides, but in $Mg(NH_3)_2(BH_4)_2$ the BH_4^- anion is ordered and instead of decomposing as the halides do to release ammonia, this diammine decomposes to release hydrogen.[51] In the lithium borohydride ammines, ammonia motion and disorder explains a number of the properties; in the case of $Li(NH_3)BH_4$ the disordered ammonia molecule shows close NH···HB contacts

which may allow the hydrogen release that has been seen by Guo et al..[102] In the diammine, it is the ammonia motion that determines the low melting temperature. While the triammine results provide less insight, the tetra-ammine shows a great deal of disorder and ammonia mobility that explains why it requires stabilisation with an ammonia vapour pressure of 110 mbar. Most of this disorder and ammonia motion has been determined through combinations of diffraction experiments and DFT calculations. Using such techniques in combination has provided a level of insight into the materials that neither could provide individually.

There are a number of areas of investigation that have been started in this Thesis where further work would strengthen the understanding of the nature of ammonia coordination in the solid state. A clear place starting point is the solution of the low-temperature crystal structures for all the compounds. The ammonia molecule orders at low temperatures, which, in turn, makes its interactions with local ions clearer; observing the subsequent phase changes and higher temperature disordering will provide a better understanding of the materials. Accurate low-temperature structures will also mean that INS data may be modelled more accurately, and this will allow for calculations that are accurate enough to reliably calculate a range of important thermodynamic properties and obtain a better understanding and assignment of the critical low energy modes seen in the INS data. Understanding of the $Li(NH_3)_nBH_4$ system will be further developed by studying $Li(NH_3)_nCl$ and $Li(NH_3)_nBr$; in particular pressure-temperature-composition studies of both halides and borohydride will help determine the nature of BH_4^- and NH_3 interactions and the presence of dihydrogen bonding.

The release of hydrogen has been observed from $Mg(NH_3)_2(BH_4)_2$ and $Li(NH_3)BH_4$ and this provides another interesting avenue of research.[51,102] If it is possible to release all the hydrogen in these materials then their hydrogen contents of 16.0 wt% and 18.2 wt% (for $Mg(NH_3)_2(BH_4)_2$ and $Li(NH_3)BH_4$ respectively) place them high in the rankings of high hydrogen content materials. While much of this Thesis has

focused on the role of the anion, the role of the cation must also be examined in more depth to understand hydrogen release. It appears that increasing the polarisation of the N−H bond may promote NH···HN interactions and facilitate hydrogen release upon heating. One route to achieve this may be to use similar cations with higher charge densities, such as Fe^{2+}, Co^{2+} or Ni^{2+} instead of Mg^{2+}. Experiments to determine the properties of these, and other, transition metal halides and borohydrides would provide an interesting comparison and help develop a deeper understanding of these systems. Isolation of transition metal borohydrides is difficult, given their high reduction potential in the presence of BH_4^-. However, synthesis of the borohydride ammines in liquid ammonia may be possible as the cation would become solvated and be protected by ammonia molecules.

In summary, this Thesis has reported the synthesis and structural characterisation of materials that have potential use as ammonia stores. The compounds $Li(NH_3)_nBH_4$ with n = 1, 2, 3 and 4 have been structurally and thermogravimetrically characterised and their properties have been explained principally in terms of ammonia mobility and hydrogen bonding interactions. It has been shown in this system that compounds have a high gravimetric ammonia density and provide an energy efficient storage system. The compounds $Mg(NH_3)_6X_2$ have also been characterised structurally and studied with a variety of techniques. In these materials, the disorder of the ammonia molecule indicates the strength of the ammonia-anion interaction. Where high levels of rotational disorder exist the anion size is the determining factor in desorption properties, when disorder decreases and ammonia-anion interactions are stronger, alternative reaction pathways become favourable. The general understanding of the magnesium halides has been improved, and magnesium borohydride has been shown as a lightweight ammonia storage material that allows for energy efficient cycling of ammonia. The study of the materials in this Thesis has shown them to be viable high density ammonia stores and produced a detailed understanding of the chemistry of solid state ammines.

Bibliography

[1] U.S. Geological Survey, Mineral Commodity Summaries, 2008, 118.

[2] W. Ostwald, patented the process known as "The Ostwald Process," as "Process of manufacturing nitric acid," in 1906.

[3] A. Saleem, "Process for the simultaneous absorption of sulfur oxides and production of ammonium sulfate," U.S. Patent 4,690,807, 1987.

[4] A. Saleem, E. Gal, G. Brown and M. M. Fredericksburg, "Process for the simultaneous absorption of sulfur oxides and production of ammonium sulfate," US Patent 5,362,458, 1994.

[5] M. Appl, *Ullmann's Encyclopedia of Industrial Chemistry: Ammonia*, Wiley-VCH Verlag GmbH & Co. KGaA, 2000.

[6] P. V. Blarigan, *Hydrogen Program Review*, U.S. Department of Energy technical report, 2000.

[7] A. Wojcik, *Journal of Power Sources*, 2003, **118**, 342–348.

[8] Q. Ma, R. Peng, Y. Lin, J. Gao and G. Meng, *Journal of Power Sources*, 2006, **161**, 95–98.

[9] C. Zamfirescu and I. Dincer, *Journal of Power Sources*, 2008, **185**, 459–465.

[10] L. Greenjr, *International Journal of Hydrogen Energy*, 1982, **7**, 355–359.

[11] W. Avery, *International Journal of Hydrogen Energy*, 1988, **13**, 761–773.

[12] P. J. Feibelman, *Physics Today*, 2005, **58**, 13.

[13] G. Thomas and G. Parks, *Potential Roles of Ammonia in a Hydrogen Economy*, U.S. Department of Energy technical report, 2006.

[14] C. Christensen, T. Johannessen, R. Sørensen and J. Nørskov, *Catalysis Today*, 2006, **111**, 140–144.

[15] A. Marko, T. Wahl, U. Alkemade, F. Brenner, M. Bareis, H. Harndorf, "Method and device for selective catalytic NOx reduction," Patent number WO09901205, January 1999.

[16] T. D. Elmøe, R. Sørensen, U. Quaade, C. H. Christensen, J. Nørskov and T. Johannessen, *Chemical Engineering Science*, 2006, **61**, 2618–2625.

[17] Air Liquide, *Gas Encyclopaedia*, `http://encyclopedia.airliquide.com/Encyclopedia.asp?GasID=2`, 2011.

[18] C. H. Christensen, R. Z. Sørensen, T. Johannessen, U. J. Quaade, K. Honkala, T. D. Elmøe, R. Køhler and J. K. Nørskov, *Journal of Materials Chemistry*, 2005, **15**, 4106–4108.

[19] E. Lepinasse, V. Goetz and G. Crosat, *Chemical Engineering and Processing*, 1994, **33**, 125–134.

[20] C. Y. Liu and K.-I. Aika, *Chemistry Letters*, 2002, **2**, 798–798.

[21] C. Y. Liu and K.-I. Aika, *Industrial & Engineering Chemistry Research*, 2004, **43**, 7484–7491.

[22] C. Y. Liu and K.-I. Aika, *Industrial & Engineering Chemistry Research*, 2004, **43**, 6994–7000.

[23] *Targets for Onboard Hydrogen Storage Systems for Light-Duty Vehicles*, U.S. Department of Energy technical report, 2009.

[24] P. W. Atkins and J. de Paula, *Atkins' Physical Chemistry*, 7th edn., 2002.

[25] C. Y. Liu and K.-I. Aika, *Bulletin of the Chemical Society of Japan*, 2004, **77**, 123–131.

[26] J. S. Hummelshøj, R. Z. Sørensen, M. Y. Kustova, T. Johannessen, J. K. Nørskov and C. H. Christensen, *Journal of the American Chemical Society*, 2006, **128**, 16–17.

[27] R. Z. Sørensen, J. S. Hummelshøj, A. Klerke, J. B. Reves, T. Vegge, J. K. Nørskov and C. H. Christensen, *Journal of the American Chemical Society*, 2008, **130**, 8660–8.

[28] W. Biltz and G. F. Hüttig, *Zeitschrift für Anorganische und Allgemeine Chemie*, 1921, **119**, 115–131.

[29] H. Zhu, X. Gu, K. Yao, L. Gao and J. Chen, *Industrial & Engineering Chemistry Research*, 2009, **48**, 5317–5320.

[30] R. W. G. Wyckoff, *Crystal Structures*, 1948, vol. III.

[31] I. Olovsson, *Acta Crystallographica*, 1965, **18**, 889–893.

[32] F. J. Ewing and L. Pauling, *Zeitschrift fuer Kristallographie, Kristallgeometrie, Kristallphysik, Kristallchemie*, 1928, **68**, 223–230.

[33] I.-C. Hwang, T. Drews and K. Seppelt, *Journal of the American Chemical Society*, 2000, **122**, 8486–8489.

[34] A. Leineweber and M. W. Friedriszik, *Journal of Solid State Chemistry*, 1999, **147**, 229–234.

[35] R. W. G. Wyckoff, *Journal of the American Chemical Society*, 1922, **44**, 1239–1245.

[36] S. H. Yü, *Nature*, 1938, **141**, 158–159.

[37] L. Asch, G. K. Shenoy, J. M. Friedt, J. P. Adloff and R. Kleinberger, *The Journal of Chemical Physics*, 1975, **62**, 2335–2342.

[38] H. Jacobs, J. Bock and C. Stüve, *Journal of the Less Common Metals*, 1987, **134**, 207–214.

[39] A. Hoser, W. Prandl, P. Schiebel and G. Heger, *Zeitschrift für Physik B: Condensed Matter*, 1990, **81**, 259–263.

[40] J. M. Newman, M. Binns, T. W. Hambley and H. C. Freeman, *Inorganic Chemistry*, 1991, **30**, 3499–3502.

[41] R. Eß man, G. Kreiner, A. Niemann, D. Rechenbach, A. Schmieding, T. Sichla, U. Zachwieja and H. Jacobs, *Zeitschrift für anorganische und allgemeine Chemie*, 1996, **622**, 1161–1166.

[42] M. H. Sørby, O. M. Løvvik, M. Tsubota, T. Ichikawa, Y. Kojima and B. C. Hauback, *Physical chemistry chemical physics: PCCP*, 2011, 2–6.

[43] J. Eckert and W. Press, *The Journal of Chemical Physics*, 1980, **73**, 451.

[44] A. Tekin, J. S. Hummelshøj, H. S. Jacobsen, D. Sveinbjörnsson, D. Blanchard, J. K. Nørskov and T. Vegge, *Energy & Environmental Science*, 2010, **3**, 448.

[45] A. Leineweber, H. Jacobs, P. Fischer and G. Böttger, *Journal of Solid State Chemistry*, 2001, **156**, 487–499.

[46] G. F. Huff, A. D. McElroy and R. M. Adams, "Electrochemical preparation of metal borohydrides," U.S. Patent 2,855,353, 1958.

[47] D. R. Schultz and R. W. Parry, *Journal of the American Chemical Society*, 1958, **80**, 4–8.

[48] K. N. Semenko, S. P. Shilkin and V. B. Polyakova, *Russian Chemical Bulletin*, 1975, **24**, 661–663.

[49] R. I. Wagner and L. R. Grant, "Magnesium borohydride diammoniate and triammoniate," U.S. Patent 4,604,271, 1986.

[50] V. N. Konoplev and T. A. Silina, *Zhurnal Neorganicheskoi Khimii (Russian Journal of Inorganic Chemistry*, 1985, **30**, 1125–1128.

[51] G. Soloveichik, J.-H. Her, P. W. Stephens, Y. Gao, J. Rijssenbeek, M. Andrus and J.-C. Zhao, *Inorganic chemistry*, 2008, **47**, 4290–8.

[52] D. J. Hunt and P. A. Cowie, Summary Report XXXI, Subcontract No. M-3181-14, St Louis U., March 31, 1955.

[53] E. A. Sullivan and S. Johnson, *Journal of Physical Chemistry*, 1959, **63**, 233–238.

[54] J. E. Huheey, E. A. Keiter and R. L. Keiter, *Inorganic Chemistry: Principles of Structure and Reactivity*, Oxford University Press, 4th edn., 1993.

[55] I. Alkorta, J. Elguero and C. Foces-Foces, *Chemical Communications*, 1996, 1633–1634.

[56] R. Custelcean and J. E. Jackson, *Chemical reviews*, 2001, **101**, 1963–1980.

[57] O. Friedrichs, F. Buchter, A. Borgschulte, A. Remhof, C. Zwicky, P. Mauron, M. Bielmann and A. Züttel, *Acta Materialia*, 2008, **56**, 949–954.

[58] A. Nickels, DPhil Thesis, University of Oxford, 2010.

[59] D. F. Shriver and M. A. Drezdzon, *The Manipulation of Air Sensitive Compounds*, John Wiley & Sons, Ltd., 2nd edn., 1986.

[60] R. Tilley, *Crystals and Crystal Structures*, John Wiley & Sons, Ltd., 2006.

[61] D. S. Sivia, *Elementary Scattering Theory For X-ray and Neutron Users*, Oxford University Press, 2011.

[62] V. F. Sears, *Neutron News*, 1992, **3**, 26–37.

[63] G. S. Pawley, *Journal of Applied Crystallography*, 1981, **14**, 357–361.

[64] H. M. Rietveld, *Journal of Applied Crystallography*, 1969, **2**, 65–71.

[65] A. Coelho, "Technical Reference TOPAS-Academic Version 4.1," 2007.

[66] A. Coelho, "TOPAS-Academic V4.1," `http://www.topas-academic.net/`, 2007.

[67] W. I. F. David, K. Shankland, J. van de Streek, E. Pidcock, W. D. S. Motherwell and J. C. Cole, *Journal of Applied Crystallography*, 2006, **39**, 910–915.

[68] P. W. Betteridge, J. R. Carruthers, R. I. Cooper, K. Prout and D. J. Watkin, *Journal of Applied Crystallography*, 2003, **36**, 1487.

[69] L. Schröder, D. J. Watkin, A. Cousson, R. I. Cooper and W. Paulus, *Journal of Applied Crystallography*, 2004, **37**, 545–550.

[70] `http://www.synchrotron.org.au`, last accessed March 2011.

[71] ID31 website, `http://www.elettra.trieste.it/`, last accessed March 2011.

[72] ID31 website, http://www.esrf.eu/UsersAndScience/Experiments/StructMaterials/ID31, last accessed April 2011.

[73] I11 website, http://www.diamond.ac.uk/Home/Beamlines/I11.html, last accessed September 2010.

[74] Private communication with Prof. A. N. Fitch.

[75] ID31 website, http://www.isis.stfc.ac.uk/aboutisis.html, last accessed November 2010.

[76] HRPD User Manual, available at http://www.isis.stfc.ac.uk/instruments/hrpd/documents/hrpd-manual6735.pdf, last accessed April 2011.

[77] A. Hannon, *Nuclear Instruments and Methods in Physics Research Section A: Accelerators, Spectrometers, Detectors and Associated Equipment*, 2005, **551**, 88–107.

[78] P. Atkins, T. Overton, J. Rourke, M. Weller and F. Armstrong, *Shriver & Atkins Inorganic Chemistry*, Oxford University Press, 4th edn., 2006.

[79] A. Brisdon, *Inorganic Spectroscopic Methods*, Oxford University Press, 2008.

[80] P. Mitchell, S. Parker, A. Ramirez-Cuesta and J. Tomkinson, *Vibrational Spectroscopy with Neutrons*, World Scientific, Singapore, 2005.

[81] http://hudsonlab.syr.edu/inss.html, last accessed December 2010.

[82] TOSCA website, http://www.isis.stfc.ac.uk/instruments/tosca/, last accessed December 2010.

[83] P. Hore, *Nuclear Magnetic Resonance*, Oxford University Press, 1998.

[84] Durham/EPSRC NMR service website, http://www.dur.ac.uk/solid.service/information/, last accessed July 2010.

[85] E. R. Andrew, *International Reviews in Physical Chemistry*, 1981, **1**, 195–224.

[86] P. Chater, P. Anderson, J. Prendergast, A. Walton, V. Mann, D. Book, W. I. F. David, S. R. Johnson and P. P. Edwards, *Journal of Alloys and Compounds*, 2007, **446-447**, 350–354.

[87] W. Koch and M. C. Holthausen, *A Chemist's Guide to Density Functional Theory*, Oxford University Press, 2nd edn., 2002.

[88] M. C. Payne, T. A. Arias and J. D. Joannopoulos, *Reviews of Modern Physics*, 1992, **64**, 1045–1097.

[89] P. Hohenberg and W. Kohn, *Physical Review B*, 1964, **136**, 864–871.

[90] W. Kohn and L. Sham, *Physical Review A*, 1965, **140**, 1133–1138.

[91] S. J. Clark, M. D. Segall, C. J. Pickard, P. J. Hasnip, M. I. J. Probert, K. Refson and M. C. Payne, *Zeitschrift für Kristallographie*, 2005, **220**, 567–570.

[92] CASTEP website, `http://www.castep.org/`, last accessed January 2011.

[93] A. Ramirez-Cuesta, *Computer Physics Communications*, 2004, **157**, 226–238.

[94] P. W. Atkins and J. de Paula, *Atkins' Physical Chemistry*, 8th edn., 2006.

[95] P. Schiebel, A. Hoser, W. Prandl, G. Heger, W. Paulus and P. Schweissl, *Journal of Physics: Condensed Matter*, 1994, **6**, 10989–11005.

[96] B. Zhong, X. Huang, G. Wen, X. Zhang, H. Bai, T. Zhang and H. Yu, *Solid State Communications*, 2010, **150**, 1552–1555.

[97] A.-M. Racu, J. Schoenes, Z. Lodziana, A. Borgschulte and A. Züttel, *The Journal of Physical Chemistry. A*, 2008, **112**, 9716–9722.

[98] E. R. Andresen, R. Gremaud, A. Borgschulte, A. J. Ramirez-Cuesta, A. Züttel and P. Hamm, *The journal of physical chemistry. A*, 2009, **113**, 12838–46.

[99] T. E. Jenkins and A. R. Bates, *Journal of Physics C: Solid State Physics*, 1981, **14**, 817–827.

[100] D. Ishikawa, *Vibrational Spectroscopy*, 1994, **8**, 87–95.

[101] A. Migdal-Mikuli, E. Mikuli and K. Zabinska, *Journal of Physics C: Solid State Physics*, 1982, **15**, 6565–6571.

[102] Y. Guo, G. Xia, Y. Zhu, L. Gao and X. Yu, *Chemical Communications*, 2010, **46**, 2599–601.

[103] H. Jacobs, H. Barlage and M. Friedriszik, *Zeitschrift für Anorganische und Allgemeine Chemie*, 2004, **630**, 645–648.

[104] N. Niimura, K. Shimaoka, H. Motegi and S. Hoshino, *Journal of the Physical Society of Japan*, 1972, **32**, 1019–1026.

[105] R. D. Shannon, *Acta Crystallographica Section A*, 1976, **32**, 751–767.

[106] D. R. Lide, *CRC Handbook of Chemistry and Physics*, 84th edn., 2003.

[107] A. F. Kapustinskii, *Quarterly Reviews, Chemical Society*, 1956, **10**, 283–294.

[108] R. Cerný, Y. Filinchuk, H. Hagemann and K. Yvon, *Angewandte Chemie (International ed. in English)*, 2007, **46**, 5765–5767.

[109] A. Zaluska, L. Zaluski and J. O. Strom-Olsen, *Journal of Alloys and Compounds*, 1999, **289**, 197–206.

[110] C. W. F. T. Pistorius, *Zeitschrift für Physikalische Chemie Neue Folge*, 1974, **88**, 253.

Appendix A

DFT Convergence Tests

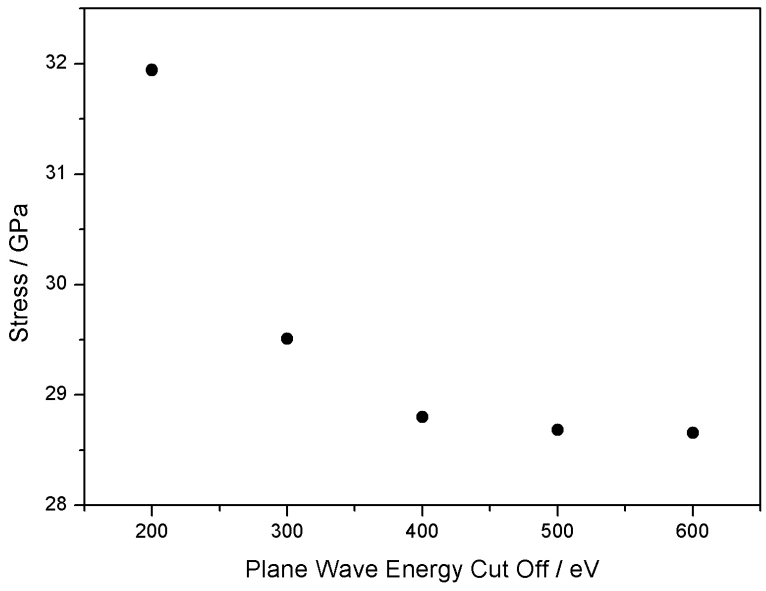

Figure A.1: The calculated stress in $Li(NH_3)BH_4$ as a function of plane wave cut-off energy

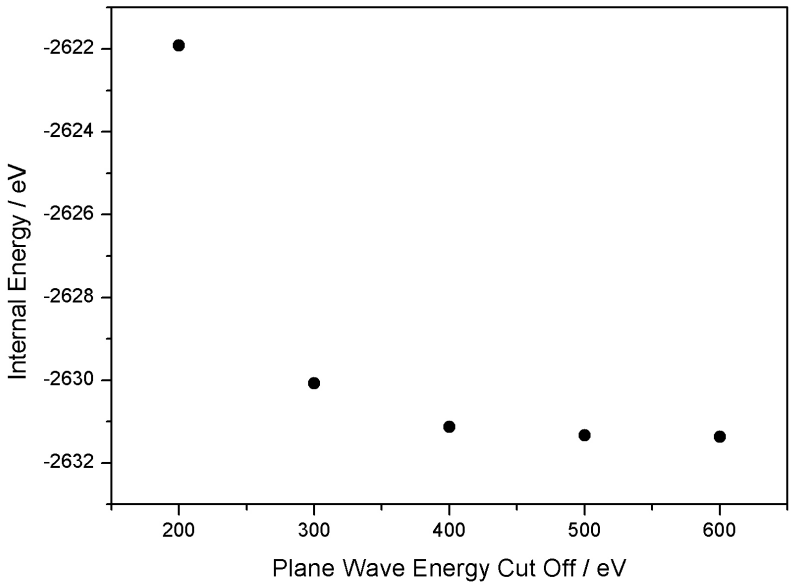

Figure A.2: The calculated internal energy of $Li(NH_3)BH_4$ as a function of plane wave cut-off energy

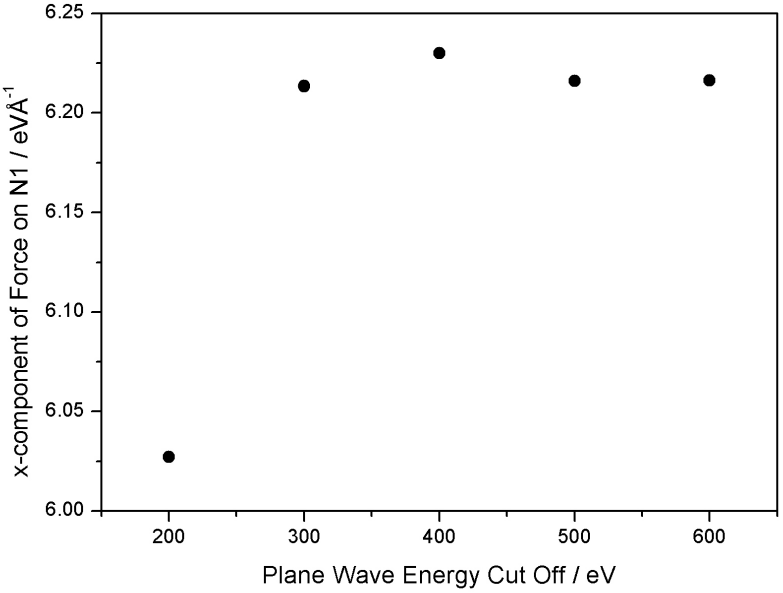

Figure A.3: The calculated x-component of the force on atom N1 in $Li(NH_3)BH_4$ as a function of plane wave cut-off energy

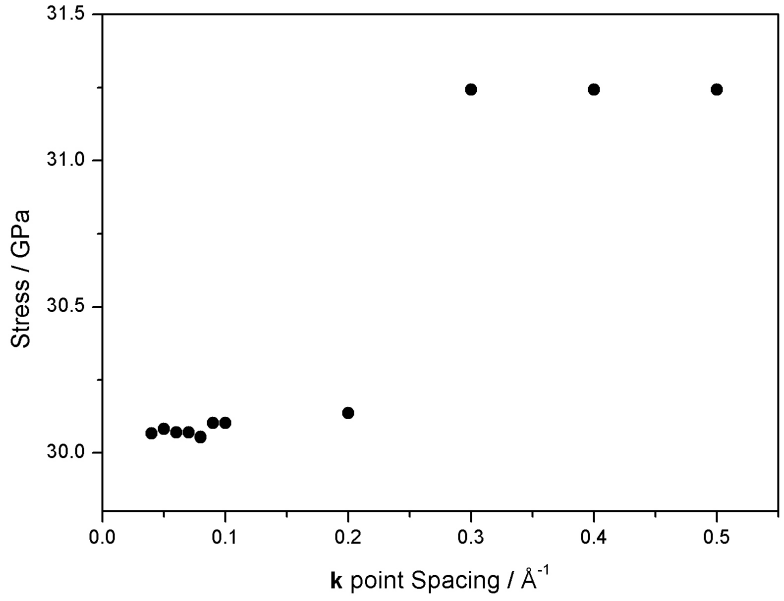

Figure A.4: The calculated stress in $Li(NH_3)BH_4$ as a function of **k**-point sampling

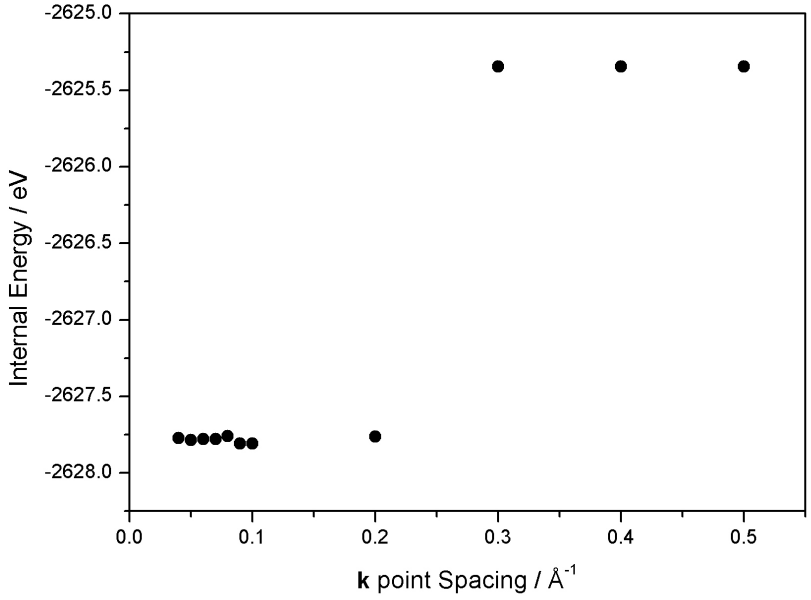

Figure A.5: The calculated internal energy of $Li(NH_3)BH_4$ as a function of **k**-point sampling

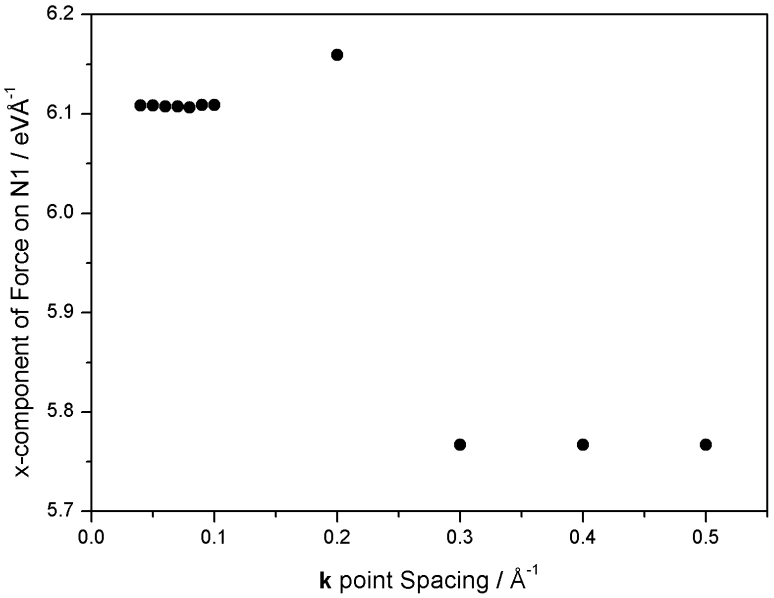

Figure A.6: The calculated x-component of the force on atom N1 in $Li(NH_3)BH_4$ as a function of **k**-point sampling

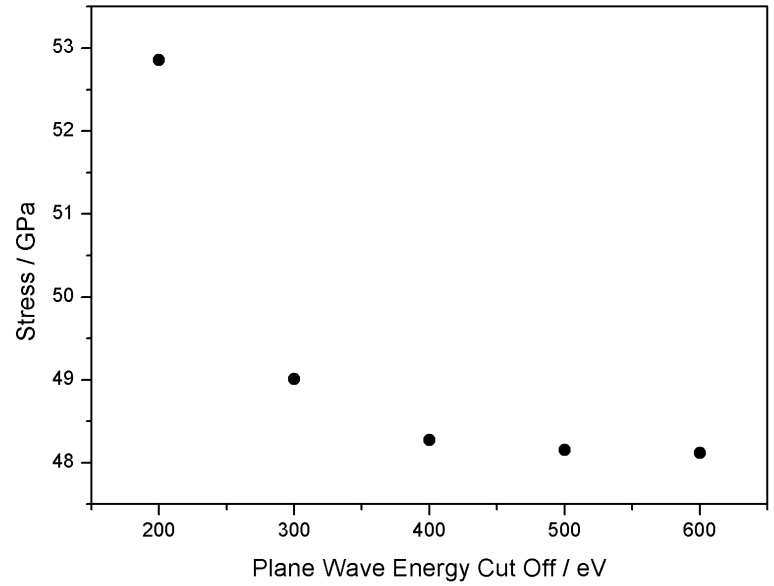

Figure A.7: The calculated stress in $Mg(NH_3)_6Cl_2$ as a function of plane wave cut-off energy

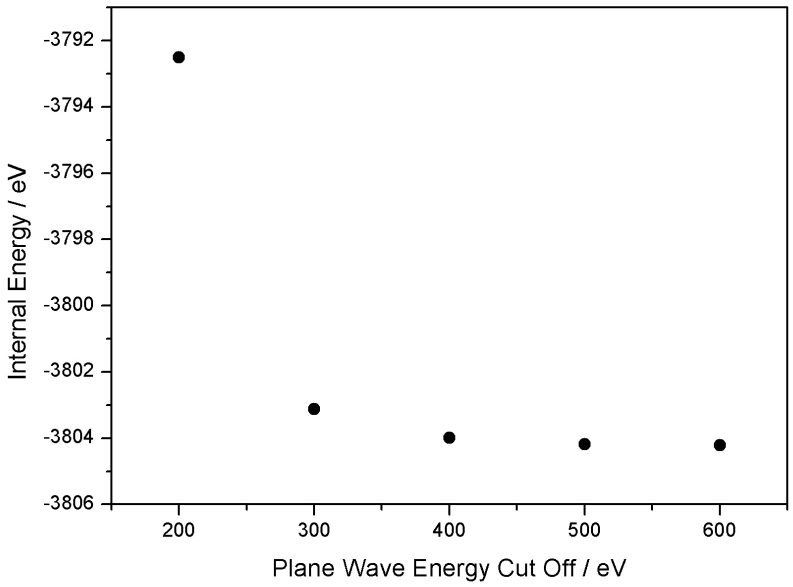

Figure A.8: The calculated internal energy of $Mg(NH_3)_6Cl_2$ as a function of plane wave cut-off energy

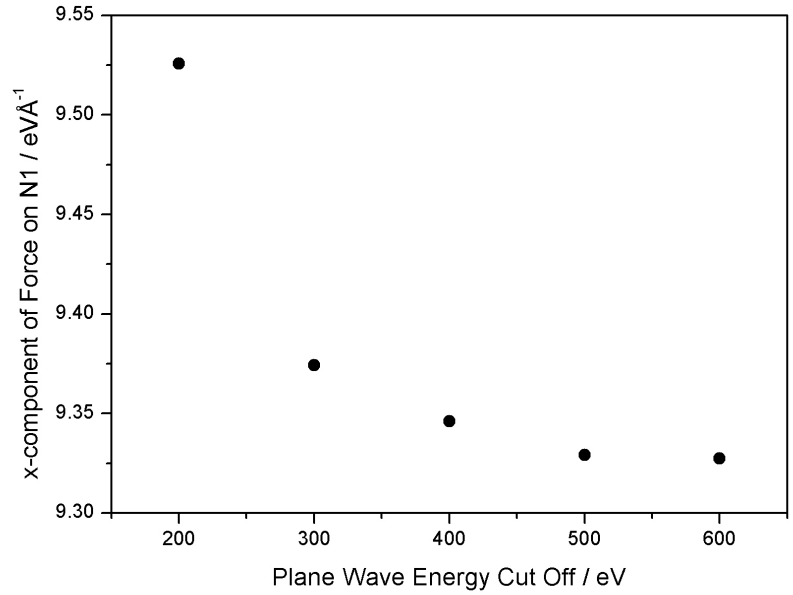

Figure A.9: The calculated x-component of the force on atom N1 in $Mg(NH_3)_6Cl_2$ as a function of plane wave cut-off energy

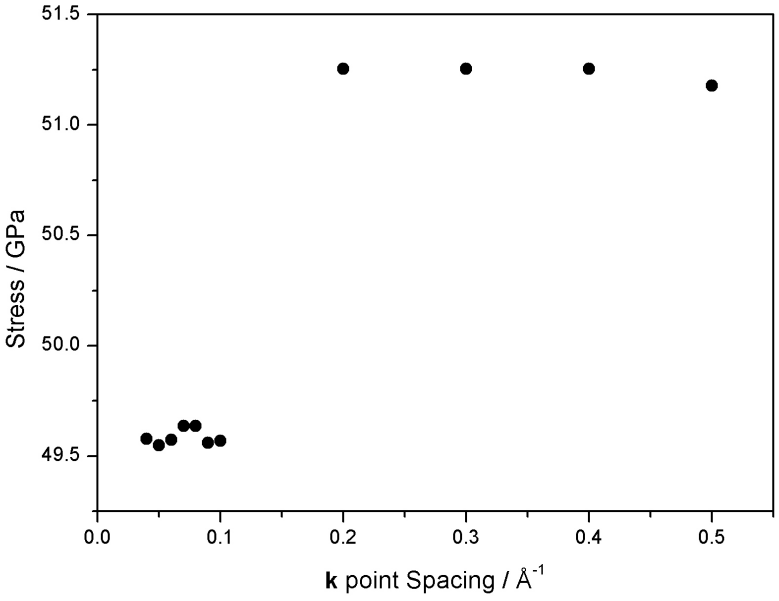

Figure A.10: The calculated stress in $Mg(NH_3)_6Cl_2$ as a function of **k**-point sampling

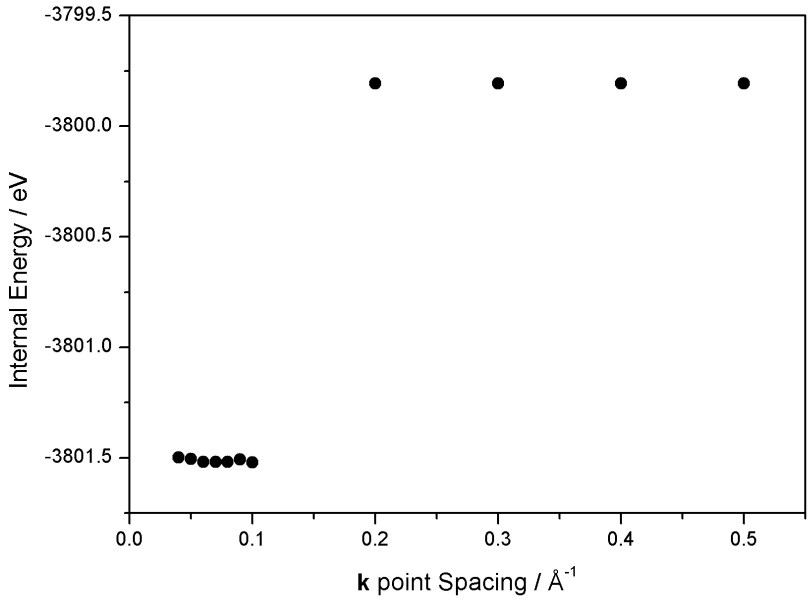

Figure A.11: The calculated internal energy of $Mg(NH_3)_6Cl_2$ as a function of **k**-point sampling

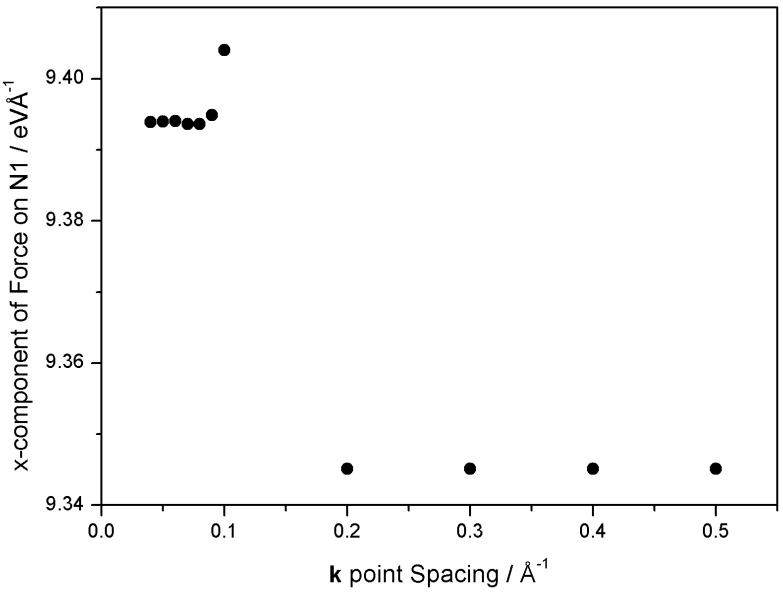

Figure A.12: The calculated x-component of the force on atom N1 in $Mg(NH_3)_6Cl_2$ as a function of **k**-point sampling

Appendix B

Lithium Borohydride Ammine Vapour Pressures

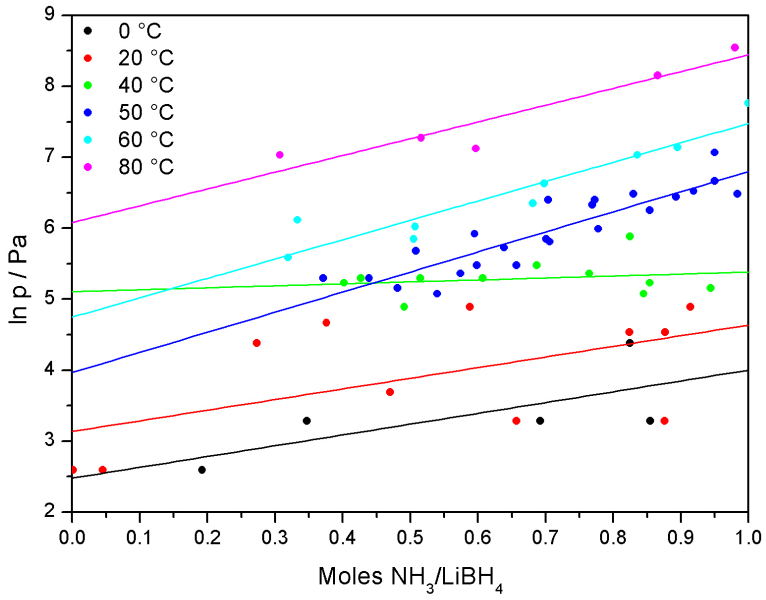

Figure B.1: The vapour pressures $Li(NH_3)_nBH_4$, n = 0-1 at various temperatures. Extracted from data reported by Sullivan and Johnson[53]

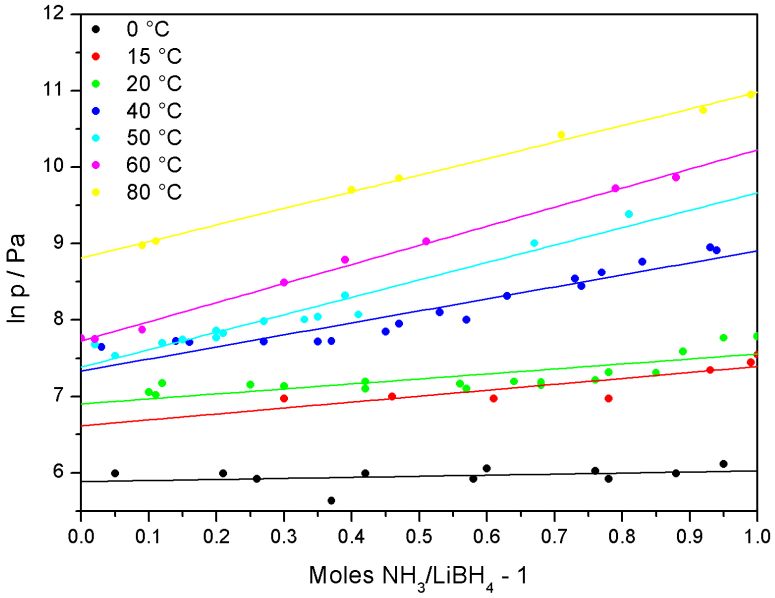

Figure B.2: The vapour pressures $Li(NH_3)_nBH_4$, n = 1-2 at various temperatures. Extracted from data reported by Sullivan and Johnson[53]

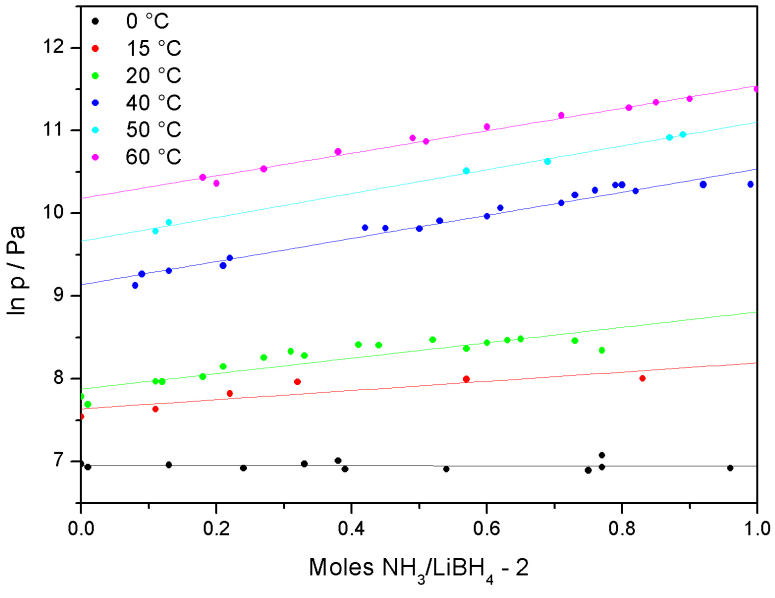

Figure B.3: The vapour pressures $Li(NH_3)_nBH_4$, n = 2-3 at various temperatures. Extracted from data reported by Sullivan and Johnson[53]

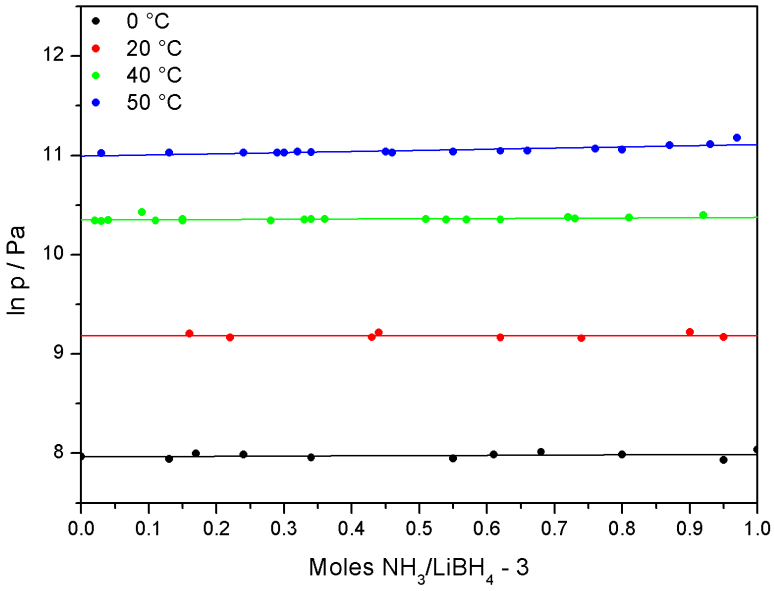

Figure B.4: The vapour pressures $Li(NH_3)_nBH_4$, n = 3-4 at various temperatures. Extracted from data reported by Sullivan and Johnson[53]

Appendix C

Script for Creating Ammonia Molecules in a Unit Cell

The script used to position hydrogen atoms of an ammonia molecule within a known unit cell given position of atoms M and N. Written in Python 2.5.4.

```
from math import *
from numpy import *
from Scientific.Geometry.Quaternion import Quaternion
# Unit cell matrix
# p = [a b c alpha beta gamma]
p = [10, 10, 10, 90, 90, 90]
a = p[0]
b = p[1]
c = p[2]
alpha = (p[3] * pi) / 180.0
beta = (p[4] * pi) / 180.0
gamma = (p[5] * pi) / 180.0
ax = a
bx = b * cos(gamma)
by = sqrt(b**2 - bx**2)
cx = c * cos(beta)
cy = (b * c * cos(alpha) - cx * bx) / by
cz = sqrt(c**2 - cx**2 - cy**2);
A = array([[ax,  0,  0],
           [bx, by,  0],
           [cx, cy, cz]])
invA = linalg.inv(A)
# this converts coordinate system with x = a
# invA * mat converts x to a
# A * mat converts a to x
```

```
# M-N vector N.B. real space from now on
M_a = array([0.3338,  0.00000,  0.8480])
N_a = array([0.360,  0.000,  0.994])
M = dot(A,M_a)
N = dot(A,N_a)
MN =  N - M
# axis and M-N vector, find the unit normal and angle
x_ax = array([1, 0, 0])
y_ax = array([0, 1, 0])
z_ax = array([0, 0, 1])
axis = z_ax
n_full = cross(axis,MN)
n_mod = sqrt(dot(n_full,n_full))
n = array([n_full[0]/n_mod, n_full[1]/n_mod, n_full[2]/n_mod])
MN_mod = sqrt(dot(MN,MN))
theta = arccos((vdot(MN, axis)) / MN_mod)
# Create quaternion and rotation matrices
w = cos(theta/2)
x = (sin(theta/2)) * n[0]
y = (sin(theta/2)) * n[1]
z = (sin(theta/2)) * n[2]
q_full = Quaternion(w,x,y,z)
q = Quaternion.normalized(q_full)
R_mem = Quaternion.asRotation(q)
R = R_mem.tensor.array
# Create hydrogen atoms
NH_bond = 0.847
MNH = 109.5
xNH = math.radians((MNH - 90))
r_angle = math.radians(62)
a_0 = r_angle
a_1 = r_angle + (2 * pi / 3)
a_2 = r_angle - (2 * pi / 3)
Rz_0 = array([[cos(a_0), -sin(a_0), 0],
              [sin(a_0), cos(a_0), 0],
              [0, 0, 1]])
Rz_1 = array([[cos(a_1), -sin(a_1), 0],
              [sin(a_1), cos(a_1), 0],
              [0, 0, 1]])
Rz_2 = array([[cos(a_2), -sin(a_2), 0],
              [sin(a_2), cos(a_2), 0],
              [0, 0, 1]])
H_base = array([(NH_bond * (cos(xNH))), 0, (NH_bond * (sin(xNH)))])
H_0 = dot(Rz_0,H_base)
H_1 = dot(Rz_1,H_base)
```

```
H_2 = dot(Rz_2, H_base)
# Rotate hydrogen vectors to face in direction MN and add to N coordinates
H_0_R = dot(R, H_0)
H_1_R = dot(R, H_1)
H_2_R = dot(R, H_2)
NH_0_R = N + H_0_R
NH_1_R = N + H_1_R
NH_2_R = N + H_2_R
# Convert H coordinates into the unit cell
H1 = dot(invA, NH_0_R)
H2 = dot(invA, NH_1_R)
H3 = dot(invA, NH_2_R)
print H1
print H2
print H3
```

Appendix D

Lithium Borohydride Ammine Phonon Modes

Table D.1: The calculated phonon modes for $Li(NH_3)BH_4$.

Number	Energy		Description
	cm^{-1}	meV	
1	-44.8	-5.56	NH_3 libration
2	-21.2	-2.63	NH_3 libration
3	-0.1	-0.01	anhormonic phonon mode
4	-0.1	-0.01	anhormonic phonon mode
5	-0.1	-0.01	anhormonic phonon mode
6	22.9	2.84	NH_3 libration
7	41.5	5.15	NH_3 libration
8	41.9	5.20	xz-plane shearing
9	67.2	8.33	xz-plane lattice vibration
10	67.7	8.40	NH_3 libration
11	68.1	8.44	xz-plane shearing
12	78.1	9.69	xz-plane shearing
13	93.5	11.60	NH_3 libration
14	97.8	12.13	NH_3 libration
15	126.3	15.66	xz-plane lattice vibration
16	132.5	16.43	NH_3 libration
17	136.5	16.93	xz-plane lattice vibration
18	136.7	16.95	xz-plane lattice vibration
19	137.6	17.06	NH_3 libration
20	142.7	17.70	xz-plane lattice vibration
21	147.0	18.23	NH_3 and BH_4 rocking [i]

Continued on next page

[i] significant Li movement

Table D.1 – continued from previous page

Number	Energy		Description
	cm^{-1}	meV	
22	147.3	18.27	NH_3 and BH_4 rocking [i]
23	174.8	21.68	xz-plane lattice vibration
24	179.3	22.23	BH_4 and NH_3 rocking [i]
25	180.4	22.36	BH_4 and NH_3 rocking [i]
26	180.5	22.38	BH_4 rocking
27	220.0	27.27	xz-plane lattice mode
28	220.9	27.39	xz-plane lattice mode
29	233.1	28.90	BH_4 rocking
30	233.2	28.92	BH_4 rocking
31	241.6	29.96	xz-plane lattice mode [i]
32	241.8	29.98	xz-plane lattice mode [i]
33	256.4	31.79	xz-plane lattice mode [i]
34	258.5	32.06	BH_4 libration
35	259.8	32.21	BH_4 libration
36	260.8	32.34	BH_4 rocking
37	262.0	32.49	BH_4 rocking
38	262.5	32.54	Li−B stretching [i]
39	322.1	39.94	NH_3 rocking [i]
40	341.7	42.37	NH_3 rocking [i]
41	395.5	49.04	BH_4 rocking
42	397.2	49.25	BH_4 rocking
43	407.4	50.51	BH_4 libration
44	407.6	50.53	BH_4 libration
45	427.2	52.97	BH_4 rocking
46	429.4	53.25	BH_4 rocking
47	430.1	53.33	NH_3 rocking
48	432.8	53.67	BH_4 libration and NH_3 rocking
49	435.9	54.05	NH_3 rocking
50	440.3	54.59	BH_4 libration and NH_3 rocking
51	447.2	55.45	BH_4 libration and NH_3 rocking
52	448.8	55.65	BH_4 libration and NH_3 rocking
53	458.7	56.88	NH_3 rocking [i]
54	460.0	57.04	BH_4 rocking [i]
55	472.4	58.57	BH_4 rocking [i]
56	474.4	58.82	Li−N bond stretch [i]
57	487.0	60.39	NH_3 rocking
58	507.8	62.97	NH_3 rocking [i]
59	512.0	63.48	NH_3 rocking
60	516.0	63.98	NH_3 rocking
61	1062.3	131.71	BH_4 umberella

Continued on next page

Table D.1 – continued from previous page

Number	Energy		Description
	cm^{-1}	meV	
62	1062.7	131.77	BH_4 umberella
63	1062.8	131.78	BH_4 wagging
64	1063.2	131.83	BH_4 wagging
65	1063.4	131.85	BH_4 umberella
66	1064.1	131.94	BH_4 umberella
67	1067.8	132.39	BH_4 wagging
68	1067.8	132.40	BH_4 wagging
69	1159.1	143.71	BH_4 and NH_3 umberella
70	1160.6	143.90	BH_4 and NH_3 umberella
71	1166.1	144.59	BH_4 umberella
72	1166.3	144.61	BH_4 umberella
73	1176.2	145.84	BH_4 and NH_3 umberella
74	1177.5	146.01	BH_4 and NH_3 umberella
75	1195.5	148.24	NH_3 umberella
76	1202.3	149.07	NH_3 umberella
77	1227.5	152.20	BH_4 bending
78	1227.6	152.21	BH_4 bending
79	1230.8	152.61	BH_4 bending
80	1230.9	152.62	BH_4 bending
81	1263.5	156.66	BH_4 bending
82	1264.7	156.81	BH_4 bending
83	1270.2	157.50	BH_4 bending
84	1270.9	157.58	BH_4 bending
85	1573.2	195.07	NH_3 wagging
86	1575.9	195.39	NH_3 wagging
87	1581.1	196.05	NH_3 wagging
88	1584.0	196.41	NH_3 wagging
89	1615.3	200.29	NH_3 clapping
90	1617.4	200.54	NH_3 clapping
91	1622.1	201.13	NH_3 clapping
92	1623.2	201.27	NH_3 flapping
93	2297.8	284.91	BH_4 stretch
94	2297.8	284.91	BH_4 stretch
95	2300.6	285.25	BH_4 stretch
96	2301.5	285.37	BH_4 stretch
97	2333.3	289.31	BH_4 stretch
98	2333.8	289.38	BH_4 stretch
99	2338.4	289.95	BH_4 stretch
100	2338.6	289.96	BH_4 stretch
101	2376.8	294.70	BH_4 stretch

Continued on next page

Table D.1 – continued from previous page

Number	Energy		Description
	cm^{-1}	meV	
102	2377.1	294.74	BH_4 stretch
103	2378.1	294.87	BH_4 stretch
104	2378.4	294.91	BH_4 stretch
105	2385.8	295.82	BH_4 stretch
106	2396.0	297.09	BH_4 stretch
107	2396.5	297.15	BH_4 stretch
108	2398.0	297.33	BH_4 stretch
109	3415.8	423.53	NH_3 stretch
110	3416.2	423.58	NH_3 stretch
111	3416.6	423.63	NH_3 stretch
112	3417.0	423.69	NH_3 stretch
113	3513.0	435.58	NH_3 stretch
114	3513.0	435.59	NH_3 stretch
115	3513.0	435.59	NH_3 stretch
116	3513.0	435.59	NH_3 stretch
117	3529.9	437.68	NH_3 stretch
118	3530.1	437.70	NH_3 stretch
119	3532.9	438.05	NH_3 stretch
120	3535.0	438.31	NH_3 stretch

Table D.2: The calculated phonon modes for $Mg(NH_3)_6Cl_2$.

Number	Energy		Description
	cm^{-1}	meV	
1	-0.1	-0.01	anhormonic phonon mode
2	-0.1	-0.01	anhormonic phonon mode
3	0.0	0.00	anhormonic phonon mode
4	76.0	9.42	acoustic lattice mode
5	88.7	11.00	acoustic lattice mode
6	107.0	13.26	acoustic lattice mode
7	117.1	14.52	acoustic lattice mode
8	123.3	15.29	acoustic lattice mode
9	134.7	16.70	acoustic lattice mode
10	154.0	19.09	Mg−N bond bending
11	176.0	21.82	Mg−N bond bending
12	177.1	21.96	Mg−N bond bending
13	187.1	23.20	Mg−N bond bending

Continued on next page

Table D.2 – continued from previous page

Number	Energy		Description
	cm^{-1}	meV	
14	207.3	25.70	Mg−N bond bending
15	224.2	27.80	Mg−N bond bending
16	229.7	28.48	Mg−N bond bending
17	234.4	29.06	Mg−N bond bending
18	238.3	29.55	Mg−N bond bending
19	239.9	29.74	Mg−N bond bending
20	247.9	30.74	Mg−N bond bending
21	259.3	32.15	Mg−N bond bending
22	262.9	32.60	Mg−N bond bending
23	285.8	35.44	Mg−N bond bending
24	312.3	38.72	NH_3 rotation
25	313.0	38.81	NH_3 rotation
26	328.8	40.77	NH_3 rotation
27	331.5	41.11	NH_3 rotation
28	339.1	42.05	NH_3 rotation
29	348.9	43.26	NH_3 rotation
30	352.9	43.76	NH_3 rotation
31	358.7	44.48	NH_3 rotation
32	361.0	44.76	NH_3 rotation
33	366.9	45.50	NH_3 rotation
34	493.8	61.22	NH_3 rocking
35	510.0	63.23	NH_3 rocking
36	533.3	66.13	NH_3 rocking
37	545.7	67.67	NH_3 rocking
38	552.7	68.53	NH_3 rocking
39	606.8	75.24	NH_3 rocking
40	616.7	76.47	NH_3 rocking
41	634.1	78.62	NH_3 rocking
42	639.6	79.31	NH_3 rocking
43	665.0	82.46	NH_3 rocking
44	672.9	83.44	NH_3 rocking
45	697.7	86.51	NH_3 rocking
46	1121.9	139.10	NH_3 umbrella
47	1143.1	141.73	NH_3 umbrella
48	1146.9	142.21	NH_3 umbrella
49	1158.7	143.67	NH_3 umbrella
50	1166.7	144.66	NH_3 umbrella
51	1196.9	148.41	NH_3 umbrella
52	1552.7	192.52	NH_3 bending
53	1561.3	193.59	NH_3 bending

Continued on next page

Table D.2 – continued from previous page

Number	Energy		Description
	cm^{-1}	meV	
54	1565.1	194.06	NH_3 bending
55	1572.1	194.93	NH_3 bending
56	1574.4	195.21	NH_3 bending
57	1587.3	196.82	NH_3 bending
58	1588.6	196.97	NH_3 bending
59	1599.1	198.28	NH_3 bending
60	1603.3	198.79	NH_3 bending
61	1609.1	199.52	NH_3 bending
62	1628.4	201.92	NH_3 bending
63	1631.5	202.30	NH_3 bending
64	3317.8	411.38	NH_3 stretch
65	3318.5	411.46	NH_3 stretch
66	3331.8	413.12	NH_3 stretch
67	3337.1	413.78	NH_3 stretch
68	3373.6	418.30	NH_3 stretch
69	3379.8	419.08	NH_3 stretch
70	3427.6	424.99	NH_3 stretch
71	3428.0	425.04	NH_3 stretch
72	3436.1	426.05	NH_3 stretch
73	3446.1	427.29	NH_3 stretch
74	3475.2	430.89	NH_3 stretch
75	3485.0	432.11	NH_3 stretch
76	3571.3	442.82	NH_3 stretch
77	3573.2	443.05	NH_3 stretch
78	3573.3	443.07	NH_3 stretch
79	3574.3	443.18	NH_3 stretch
80	3584.5	444.45	NH_3 stretch
81	3585.6	444.58	NH_3 stretch

Table D.3: The calculated phonon modes for $Li(NH_3)_2BH_4$.

Number	Energy		Description		
	cm^{-1}	meV	BH_4	NH_3, N(1)	NH_3, N(2)
1	-0.1	-0.01	— anhormonic phonon mode —		
2	-0.1	-0.01	— anhormonic phonon mode —		
3	0.0	-0.01	— anhormonic phonon mode —		
4	17.7	2.19	— acoustic NH_3 translation —		

Continued on next page

Table D.3 – continued from previous page

Number	Energy		Description		
	cm^{-1}	meV	BH_4	NH_3, N(1)	NH_3, N(2)
5	28.3	3.51	— acoustic NH_3 translation —		
6	40.4	5.01	— acoustic NH_3 translation —		
7	44.4	5.50	— acoustic —		
8	54.5	6.76	— acoustic lattice shearing —		
9	58.2	7.22	— acoustic lattice shearing —		
10	61.6	7.64	— acoustic lattice shearing —		
11	63.0	7.82	— acoustic —		
12	70.7	8.76	— acoustic with N(2) rocking —		
13	72.8	9.03	— acoustic —		
14	79.6	9.87	— acoustic —		
15	83.6	10.36	— acoustic —		
16	93.0	11.53	— acoustic with N(2) rocking —		
17	94.4	11.71			translation
18	106.1	13.16	— acoustic —		
19	107.4	13.32	— acoustic —		
20	119.1	14.76	— acoustic —		
21	121.3	15.04	— acoustic —		
22	128.2	15.90	— acoustic —		
23	128.5	15.93			rotation
24	129.8	16.09	— acoustic with N(2) breathing —		
25	130.7	16.21			rotation
26	134.7	16.71	— acoustic —		
27	145.2	18.01	— acoustic with N(2) translation —		
28	158.8	19.69	— acoustic with N(2) translation —		
29	160.9	19.95	rotation		rotation
30	161.9	20.07	rotation with significant Li movement		
31	168.8	20.93			rotation
32	169.0	20.95			rotation
33	170.4	21.12			rotation
34	172.9	21.44	— acoustic with N(2) translation —		
35	179.0	22.19			rotation
36	181.9	22.55	— acoustic with N(2) translation —		
37	193.3	23.97	rotation		rocking
38	193.8	24.03	rotation		rotation
39	196.3	24.34	rocking		
40	197.4	24.48			rocking
41	198.3	24.59	rocking		
42	201.7	25.01	rotation		
43	211.7	26.25	rocking	rotation	rocking
44	212.2	26.31	rocking	rotation	rocking

Continued on next page

Table D.3 – continued from previous page

Number	Energy		Description		
	cm^{-1}	meV	BH_4	NH_3, N(1)	NH_3, N(2)
45	212.9	26.40		rotation	bending
46	215.1	26.67	— acoustic —		
47	225.4	27.95	— acoustic —		
48	226.1	28.03		rotation	rocking
49	229.9	28.50	— acoustic —		
50	232.8	28.87	— acoustic —		
51	244.0	30.25	Li−B stretch		
52	244.9	30.36	Li−B stretch		
53	244.9	30.37	Li−B bend	Li−N bend	
54	246.6	30.57	Li−B bend	Li−N bend	
55	277.3	34.38	Li−B bend	Li−N bend	
56	292.4	36.25		rotation	
57	292.9	36.31	Li−B bend	Li−N bend	
58	293.6	36.41		rotation	rocking
59	302.9	37.56		rotation	rocking
60	306.6	38.02		rotation	rocking
61	366.0	45.38	rocking		rocking
62	370.3	45.92	rocking		
63	370.5	45.94	rotation		
64	372.0	46.13		rocking	rocking
65	373.5	46.32	rocking		rocking
66	375.7	46.59	rotation		
67	390.0	48.36	rocking		rocking
68	391.1	48.49	rocking		
69	397.6	49.30			rocking
70	400.4	49.64	rocking		rocking
71	417.6	51.78	rotation		
72	419.9	52.06	rotation		
73	471.7	58.48		Li−N stretch	
74	474.6	58.84		Li−N stretch	
75	477.0	59.14		Li−N stretch	
76	482.6	59.83		Li−N stretch	
77	497.0	61.63		rocking	
78	508.3	63.02		rocking	rocking
79	517.7	64.19		rocking	
80	519.7	64.44		rocking	rocking
81	567.6	70.38		rocking	rocking
82	568.1	70.45		rocking	rocking
83	568.5	70.49		rocking	rocking
84	569.6	70.63		rocking	rocking

Continued on next page

Table D.3 – continued from previous page

Number	Energy		Description		
	cm^{-1}	meV	BH_4	NH_3, N(1)	NH_3, N(2)
85	1057.3	131.09	umbrella		
86	1057.5	131.12	umbrella		
87	1061.1	131.57	umbrella		
88	1061.1	131.57	umbrella		
89	1062.7	131.76	umbrella		
90	1064.0	131.93	umbrella		
91	1066.1	132.19	umbrella		
92	1066.3	132.22	umbrella		
93	1095.9	135.89			umbrella
94	1105.7	137.10			umbrella
95	1106.1	137.15			umbrella
96	1107.0	137.25			umbrella
97	1156.0	143.33	umbrella		
98	1156.7	143.42	umbrella		
99	1156.8	143.43	umbrella		
100	1156.9	143.45	umbrella		
101	1192.8	147.90		umbrella	
102	1193.4	147.97		umbrella	
103	1198.8	148.65		umbrella	
104	1209.3	149.95		umbrella	
105	1229.4	152.43	clapping		
106	1229.4	152.44	clapping		
107	1233.1	152.89	clapping		
108	1233.1	152.90	clapping		
109	1264.6	156.80	clapping		
110	1264.7	156.81	clapping		
111	1268.9	157.33	clapping		
112	1269.1	157.36	clapping		
113	1566.4	194.22			clapping
114	1567.5	194.35			clapping
115	1586.1	196.67			clapping
116	1587.7	196.86			clapping
117	1603.4	198.81		clapping	clapping
118	1605.3	199.05		clapping	clapping
119	1605.6	199.08		clapping	
120	1607.8	199.36		clapping	clapping
121	1611.4	199.80		clapping	clapping
122	1612.4	199.93		clapping	clapping
123	1612.6	199.95		clapping	clapping
124	1615.2	200.28		clapping	clapping

Continued on next page

Table D.3 – continued from previous page

Number	Energy		Description		
	cm^{-1}	meV	BH_4	NH_3, N(1)	NH_3, N(2)
125	1651.3	204.75		clapping	clapping
126	1654.2	205.11		clapping	clapping
127	1656.0	205.33		clapping	clapping
128	1659.0	205.70		clapping	clapping
129	2284.8	283.30	stretching		
130	2285.2	283.34	stretching		
131	2289.5	283.88	stretching		
132	2289.5	283.89	stretching		
133	2340.1	290.16	stretching		
134	2340.4	290.19	stretching		
135	2343.9	290.62	stretching		
136	2346.6	290.96	stretching		
137	2365.0	293.24	stretching		
138	2365.0	293.24	stretching		
139	2365.4	293.29	stretching		
140	2365.4	293.29	stretching		
141	2379.0	294.98	stretching		
142	2381.8	295.33	stretching		
143	2382.1	295.36	stretching		
144	2384.2	295.62	stretching		
145	3356.1	416.13		stretching	
146	3356.3	416.16		stretching	
147	3356.7	416.21		stretching	
148	3358.8	416.47		stretching	
149	3411.2	422.97			stretching
150	3411.3	422.98			stretching
151	3414.9	423.42			stretching
152	3415.2	423.46			stretching
153	3431.9	425.53			stretching
154	3431.9	425.53		stretching	
155	3432.0	425.54		stretching	
156	3432.0	425.54		stretching	
157	3515.1	435.85			stretching
158	3515.2	435.86			stretching
159	3515.3	435.87			stretching
160	3515.4	435.89			stretching
161	3534.5	438.26		stretching	
162	3534.7	438.27		stretching	
163	3534.9	438.31		stretching	
164	3535.1	438.32		stretching	

Continued on next page

Table D.3 – continued from previous page

Number	Energy		Description		
	cm^{-1}	meV	BH_4	NH_3, N(1)	NH_3, N(2)
165	3549.9	440.16			stretching
166	3549.9	440.16			stretching
167	3551.3	440.33			stretching
168	3551.3	440.34			stretching

Appendix E

Additional Data

Table E.1: The atomic coordinates obtained from the Rietveld refinement of the ordered model of $Li(NH_3)BH_4$ against X-ray powder diffraction data.

atom	site	x	y	z	B_{iso}
N	N1	0.597	0.750	0.650	7.58
B	B1	0.907	0.750	0.398	5.61
Li	Li1	0.882	0.750	0.575	5.03
H	H1	0.726	0.750	0.446	5.61
H	H2	0.072	0.750	0.451	5.61
H	H3	0.901	0.526	0.354	5.61
H	H4	0.516	0.573	0.636	7.58
H	H5	0.612	0.750	0.716	7.58

Table E.2: The atomic coordinates obtaind from the Rietveld refinement of the disordered model of $Mg(NH_3)_6Cl_2$ against X-ray powder diffraction data.

atom	site	x	y	z	occ.	B_{iso}
Mg	Mg1	0	0	0	1	2.24(4)
Cl	Cl1	0.25	0.25	0.25	1	3.7(3)
N	N1	0	0	0.2140(2)	1	4.2(6)
H	H1	-0.074(1)	0	0.2426(9)	0.125	4.2(6)
H	H2	-0.072(1)	-0.0192(3)	0.2426(9)	0.125	4.2(6)
H	H3	-0.0641(8)	-0.0370(5)	0.2426(9)	0.125	4.2(6)
H	H4	-0.0524(7)	-0.0524(7)	0.2426(9)	0.125	4.2(6)

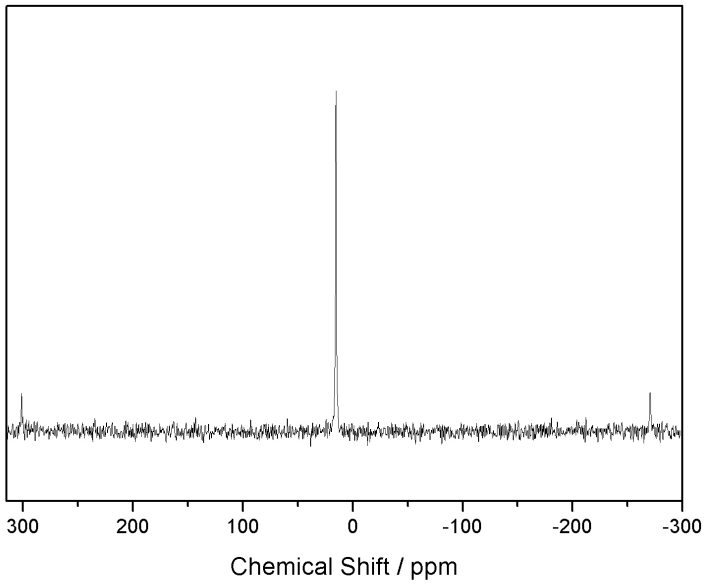

Figure E.1: The ^{25}Mg NMR spectra of $Mg(NH_3)_6Br_2$, showing a sharp line at 15.245 ppm (referenced to a 1 M solution of $Mg(H_2O)_6Cl_{2\,(aq)}$).

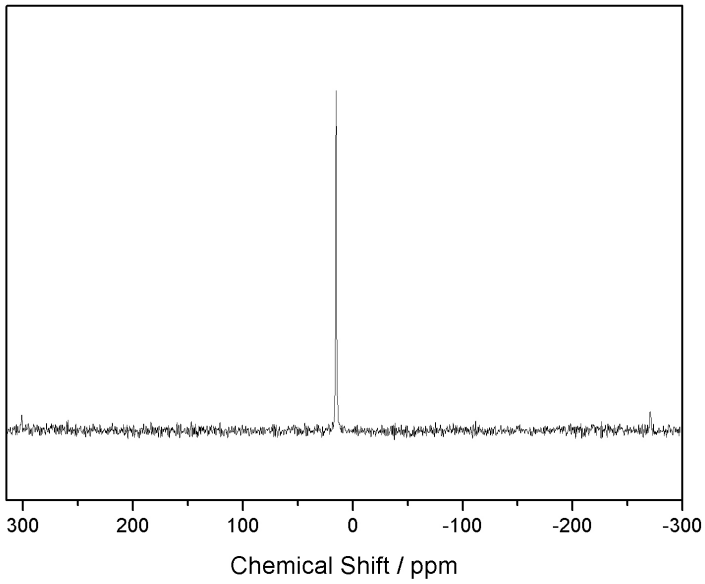

Figure E.2: The ^{25}Mg NMR spectra of $Mg(NH_3)_6I_2$, showing a sharp line at 15.095 ppm (referenced to a 1 M solution of $Mg(H_2O)_6Cl_{2\,(aq)}$).

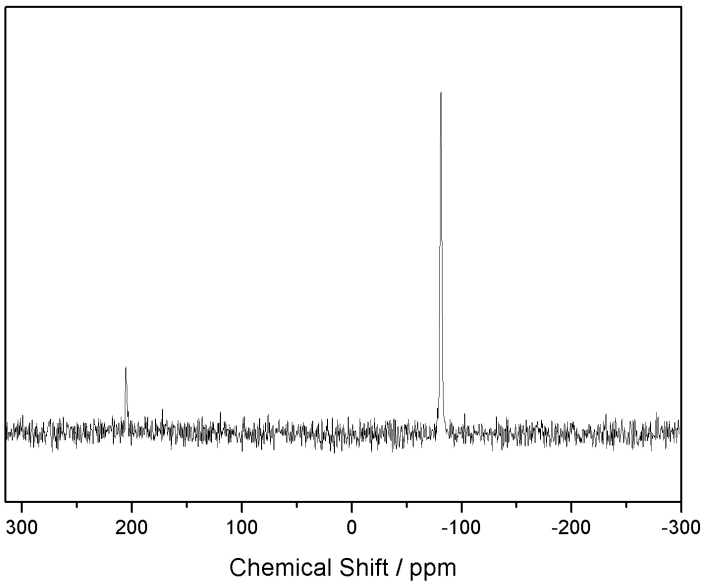

Figure E.3: The ^{25}Mg NMR spectra of MgI_2, showing a sharp line at -81.109 ppm (referenced to a 1 M solution of $Mg(H_2O)_6Cl_{2\,(aq)}$).

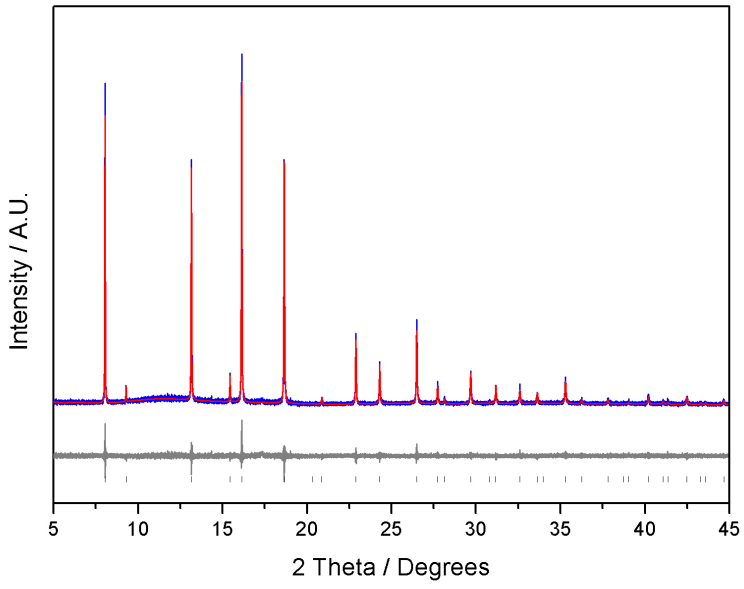

Figure E.4: Final fit to the data for Rietveld refinement of the $Mg(NH_3)_6Cl_2$ model to X-ray powder diffraction data collected at the Diamond Light Source with a wavelength $\lambda = 0.82000$ Å. Experimental data are shown in blue, calculated in red with the difference in grey, tick marks show the expected positions of Bragg reflections.

Table E.3: The atomic coordinates obtained from Rietveld refinement of the disordered model of $Mg(NH_3)_6Br_2$ against X-ray diffraction data.

atom	site	x	y	z	occ.	B_{iso}
Mg	Mg1	0	0	0	1	2.50(7)
Br	Br1	0.25	0.25	0.25	1	3.54(3)
N	N1	0	0	0.2082(3)	1	3.2(1)
H	H1	-0.078(1)	0	0.245(2)	0.125	3.2(1)
H	H2	-0.076(1)	-0.0202(4)	0.245(2)	0.125	3.2(1)
H	H3	-0.068(1)	-0.0392(7)	0.245(2)	0.125	3.2(1)
H	H4	-0.055(1)	-0.055(1)	0.245(2)	0.125	3.2(1)

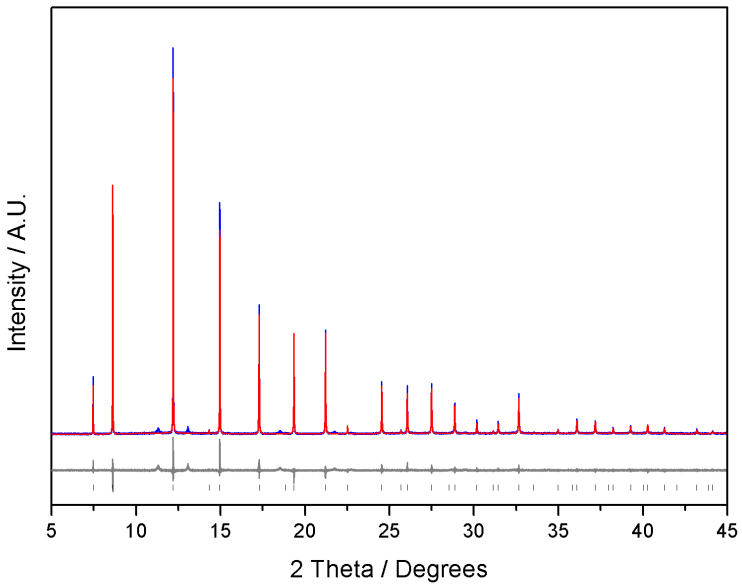

Figure E.5: Final fit to the data for Rietveld refinement of the $Mg(NH_3)_6I_2$ model to X-ray powder diffraction data collected at the Diamond Light Source with a wavelength $\lambda = 0.82000$ Å. Experimental data are shown in blue, calculated in red with the difference in grey, tick marks show the expected positions of Bragg reflections.

Table E.4: The atomic coordinates from the Rietveld refinement of the disordered model of $Mg(NH_3)_6I_2$ against X-ray diffraction data.

atom	site	x	y	z	occ.	B_{is}
Mg	Mg1	0	0	0	1	2.37(9)
I	I1	0.25	0.25	0.25	1	3.53(2)
N	N1	0	0	0.1998(3)	1	2.5(1)
H	H1	-0.075(2)	0	0.235(2)	0.125	2.5(1)
H	H2	-0.072(2)	-0.0193(4)	0.235(2)	0.125	2.5(1)
H	H3	-0.065(1)	-0.0374(8)	0.235(2)	0.125	2.5(1)
H	H4	-0.053(1)	-0.053(1)	0.235(2)	0.125	2.5(1)

Table E.5: The atomic coordinates obtained from Rietveld refinement of the disordered model of $Li(NH_3)_4BH_4$ against neutron diffraction data.

atom	site	x	y	z	occ.
Li	Li1	0.9887	0.2500	0.6847	1.0
B	B1	0.2930	0.2500	0.3816	1.0
D	H24a	0.2932	0.2500	0.5051	0.26
D	H25a	0.1958	0.2500	0.3406	0.26
D	H26a	0.3416	0.3920	0.3403	0.26
D	H24b	0.2929	0.2500	0.2582	0.74
D	H25b	0.3902	0.2500	0.4227	0.74
D	H26b	0.2445	0.1080	0.4230	0.74
N	N1	0.8990	0.2500	0.5210	1.0
D	H1a	0.9453	0.2500	0.4407	0.40
D	H2b	0.8506	0.1396	0.5150	0.40
D	H1a	0.8191	0.2500	0.5398	0.60
D	H2b	0.9137	0.1396	0.4655	0.60
N	N2	0.1565	0.2500	0.7133	1.0
D	H4a	0.1763	0.2500	0.8080	0.40
D	H6a	0.1923	0.3604	0.6737	0.40
D	H4b	0.1976	0.2500	0.6290	0.60
D	H6b	0.1816	0.1396	0.7632	0.60
N	N3	0.9313	0.4659	0.8234	1.0
D	H10a	0.9751	0.4679	0.9057	0.40
D	H11a	0.9360	0.5922	0.7851	0.40
D	H12a	0.8536	0.4472	0.8498	0.40
D	H10b	0.9896	0.5577	0.8439	0.60
D	H11b	0.8681	0.5370	0.7881	0.60
D	H12b	0.9072	0.4126	0.9087	0.60

Table E.6: The atomic coordinates obtained from the rough geometry optimisation of $Mg(NH_3)_6Cl_2$, space group Cm, a = 10.1226 Å, b = 7.1578 Å, $\alpha = \gamma = 90$ ° $\beta = 135$ °.

atom	site	x	y	z
H	H1	-0.67440	0.41801	-1.85474
H	H2	0.31397	0.91763	-0.51246
H	H3	0.32942	0.25908	-1.17330
H	H4	-0.46624	0.23599	-1.07592
H	H5	0.52264	0.24239	-0.85312
H	H6	-0.18740	0.41769	-1.86944
H	H7	-0.18035	0.08219	-1.49890
N	N8	0.47061	0.28187	-1.02730
Cl	Cl1	-0.00844	0.25236	-0.51138
H	H10	0.16106	0.50000	-0.13814
H	H11	0.69522	0.50000	-0.46686
H	H12	0.69027	0.50000	-0.15352
H	H13	0.15863	0.50000	-1.53636
N	N14	-0.69993	0.50000	-1.96288
N	N15	-0.26785	0.50000	-0.56858
N	N16	-0.26985	0.50000	-1.97580
N	N17	-0.70360	0.50000	-1.43942
Mg	Mg1	0.49643	0.50000	-0.00532

Table E.7: The atomic coordinates obtained from the rough geometry optimisation of $Mg(NH_3)_6Br_2$, space group Cm, a = 10.4069 Å, b = 7.3588 Å, $\alpha = \gamma = 90$ ° $\beta = 135$ °.

atom	site	x	y	z
H	H1	-0.67935	0.42030	-1.87102
H	H2	0.30438	0.92014	-0.51562
H	H3	0.34119	0.26237	-1.15916
H	H4	-0.46426	0.24565	-1.07702
H	H5	0.53412	0.24627	-0.85098
H	H6	-0.19578	0.42015	-1.87762
H	H7	-0.18080	0.07970	-1.48902
N	N8	0.47766	0.28714	-1.02192
Br	Br1	-0.00541	0.25165	-0.50558
H	H10	0.16570	0.50000	-0.14770
H	H11	0.68206	0.50000	-0.48368
H	H12	0.68088	0.50000	-0.15438
H	H13	0.16541	0.50000	-1.51960
N	N14	-0.70037	0.50000	-1.97350
N	N15	-0.27683	0.50000	-0.57610
N	N16	-0.27714	0.50000	-1.97914
N	N17	-0.70105	0.50000	-1.42766
Mg	Mg1	0.49787	0.50000	-0.00236

Table E.8: The atomic coordinates obtained from the rough geometry optimisation of $Mg(NH_3)_6I_2$, space group Cm, a = 10.9149 Å, b = 7.7180 Å, $\alpha = \gamma = 90$ ° $\beta = 135$ °.

atom	site	x	y	z
H	H1	-0.68987	0.42439	-1.90310
H	H2	0.28284	0.92399	-0.53386
H	H3	0.41221	0.25481	-1.16852
H	H4	-0.37948	0.26358	-0.90660
H	H5	0.47098	0.26293	-0.90274
H	H6	-0.21770	0.42418	-1.90548
H	H7	-0.18928	0.07567	-1.48028
N	N8	0.49817	0.29567	-0.99836
I	I1	-0.01451	0.24891	-0.51930
H	H10	0.16960	0.50000	-0.16700
H	H11	0.65929	0.50000	-0.51656
H	H12	0.65827	0.50000	-0.16974
H	H13	0.17151	0.50000	-1.49498
N	N14	-0.70429	0.50000	-1.99706
N	N15	-0.29577	0.50000	-0.59730
N	N16	-0.29678	0.50000	-1.99910
N	N17	-0.70277	0.50000	-1.41418
Mg	Mg1	0.49423	0.50000	-0.00760

Table E.9: The atomic coordinates obtained from the rough geometry optimisation of $Mg(NH_3)_2Cl_2$, space group $Amm2$, a = 3.7550 Å, b = 8.2067 Å, c = 8.1810 Å.

atom	site	x	y	z
H	H1	0.78403	0.69122	-0.06225
H	H2	1.00000	0.68082	-0.88670
N	N3	1.00000	0.26274	-0.99936
Mg	Mg1	0.00000	-0.00000	-0.99316
Cl	Cl1	0.50000	-0.00000	-0.20761
Cl	Cl2	0.50000	1.00000	-0.77812

Table E.10: The atomic coordinates obtained from the rough geometry optimisation of $Mg(NH_3)_2Br_2$, space group $P1$, a = 5.9440 Å, b = 11.8760 Å, c = 3.9830 Å.

atom	site	x	y	z
H	H1	0.89849	0.40160	0.13555
H	H2	0.70736	0.30143	0.11869
H	H3	0.81927	0.35040	0.77038
H	H4	0.60179	0.89919	0.14217
H	H5	0.79438	0.80008	0.11726
H	H6	0.68207	0.85219	0.77303
H	H7	0.39755	0.10021	0.14461
H	H8	0.20648	0.20004	0.11780
H	H9	0.32047	0.14778	0.77479
H	H10	0.09957	0.59891	0.85136
H	H11	0.29050	0.69912	0.86751
H	H12	0.18283	0.64832	0.21675
N	N13	0.25870	0.12570	0.00754
N	N14	0.74184	0.87434	0.00685
N	N15	0.24040	0.62520	0.98253
N	N16	0.75908	0.37474	0.00202
Mg	Mg1	0.99989	0.00023	0.99727
Mg	Mg2	0.49984	0.50004	0.99187
Br	Br1	0.27821	0.38582	0.48762
Br	Br2	0.72109	0.61433	0.49288
Br	Br3	0.22188	0.88587	0.50299
Br	Br4	0.77831	0.11446	0.49856

Table E.11: The atomic coordinates obtained from the rough geometry optimisation of $Mg(NH_3)_2I_2$, space group $P1$, a = 6.2850 Å, b = 12.5590 Å, c = 4.3020 Å.

atom	site	x	y	z
H	H1	0.62604	0.90719	0.86427
H	H2	0.80503	0.81211	0.89806
H	H3	0.69517	0.86415	0.21199
H	H4	0.87675	0.40673	0.14293
H	H5	0.69787	0.31184	0.10337
H	H6	0.37599	0.09502	0.14215
H	H7	0.19691	0.18986	0.10412
H	H8	0.30836	0.13689	0.79266
H	H9	0.80976	0.36522	0.79283
H	H10	0.12707	0.59456	0.86551
H	H11	0.30630	0.68965	0.89654
H	H12	0.19723	0.63836	0.21206
N	N13	0.24716	0.11859	0.00880
N	N14	0.75539	0.88312	0.99576
N	N15	0.25679	0.61888	0.99583
N	N16	0.74817	0.38324	0.00894
Mg	Mg1	0.00135	0.00079	0.00247
Mg	Mg2	0.50249	0.50109	0.00284
I	I1	0.27209	0.38117	0.49718
I	I2	0.73282	0.62092	0.50803
I	I3	0.23171	0.88095	0.50776
I	I4	0.77127	0.12075	0.49695